2005

Spin models for the single molecular magnet Mn12-AC

Mohamad A. Al-Saqer
Iowa State University

Spin Models for the single molecular magnet Mn12-AC

by

Mohamad A. Al-Saqer

A dissertation submitted to the graduate faculty

in partial fulfillment of the requirements for the degree of

DOCTOR OF PHILOSOPHY

Major: Condensed Matter Physics

Program of Study Committee:
Bruce N. Harmon, Major Professor
David A. Carter-Lewis
Gordon Miller
Joerg Schmalian
Paul Canfield

Iowa State University

Ames, Iowa

2005

Graduate College
Iowa State University

This is to certify that the doctoral dissertation of

Mohamad A. Al-Saqer

has met the dissertation requirements of Iowa State University

Signature was redacted for privacy.

Major Professor

Signature was redacted for privacy.

For the Major Program

Contents

LIST OF TABLES v

LIST OF FIGURES vii

CHAPTER 1 Introduction 1

CHAPTER 2 Single-spin Model Of The Molecule Mn12-AC 4

2.1 Overview of Mn12-AC magnetic molecule 5

2.2 Double-well energy potential 8

2.3 Quantum tunneling of magnetism and selection rules in Mn12-AC 10

2.4 Lower symmetry terms in Mn12-AC 14

2.5 Effect of different perturbation terms on tunneling properties. 19

CHAPTER 3 ^{55}Mn Magnetic relaxation in Mn12-AC 24

3.1 Nuclear-Spin system Hamiltonian 30

3.2 ^{55}Mn nuclear magnetic relaxation dependence on applied field 33

CHAPTER 4 Tunneling Splitting Calculations and Truncation of Hilbert Space 43

4.1 The 8-Spin model and calculation of tunneling splittings 45

4.2 Numerical scheme of truncation of Hilbert space 49

4.3 Results 53

4.4 Discussion 54

CHAPTER 5 Exchange Couplings For The Full Spin Model 58

5.1 Exchanges as published up to date. 59

5.2 The Heisenberg Hamiltonian for Mn12-AC 62

5.3 Effect of single-ion anisotropies on Exchange Hamiltonian. 64

CHAPTER 6 General Summary 73

BIBLIOGRAPHY 75

List of Tables

2.1 Mn-Mn distances for the different exchange couplings in Mn12-AC. 5

2.2 Calculated Mn(II) and Mn(III) Manganese parameters corresponding to the single ion anisotropy terms: $-DS_{i,z}^2 + E\left(S_{i,x}^2 - S_{i,y}^2\right)$. δ represents the angle between the crystal's easy axis, c, and the longest axis of the octahedral environment surrounding the Mn^{3+} ions (see figure 2.5). 17

2.3 Calculated magnetic anisotropy and tunnel splitting of the isomers of Mn12-AC. Table and caption are cited from Ref. [23]. . . 19

4.1 Number of possible configurations for each M block of the exchange Hamiltonian for the 8−spin model. 50

5.1 The exchange coupling parameters suggested by previous authors. Except in the set LDA+U , it is assumed that $J_2' = J_2$, $J_3' = J_3$, and $J_4' = J_4$. Positive exchanges are antiferromagnetic. . 61

5.2 The results of diagonalizing Eq. (5.1) using exchange parameters listed in table 5.1. The total spin, S, and the degeneracy, d, are shown in the table next to energies. Energies are in Kelvins Results of previous authors are shown in square brackets only in case of discrepancy with our results. Question marks indicates that results were not reported by previous authors. 63

5.3 Magnetic anisotropy along crystal's easy axis for the four inequivalent site of Mn^{3+} ions. 65

5.4 The expectation value of the moment, $\langle S_z^i \rangle / S_i$, in the ground state calculated using eigenvectors of the exchange Hamiltonian 5.1 (column a for each Mn ion type) and the Hamiltonian 5.2 (column b) using each of the five exchange sets in table 5.1 and anisotropies in table 2.2 (for the isomer n=2 trans). For comparison, listed are the results from references: [11] polarized neutron diffraction experiment (PND), [32] ^{55}Mn nuclear magnetic resonance (NMR), and [66] calculations based on the density functional theory (DFT). 66

List of Figures

1.1 Hysteresis loops at low temperatures show sudden jumps of magnetization at regularly spaced intervals (see inset) of the applied magnetic field. Figure is cited from [1]. 2

2.1 The magnetic Molecule Mn12-AC viewed slightly off symmetry axis c. In this figure only the Mn, Oxygen and Carbon ions are shown. Hydrogens were omitted for simplicity. 6

2.2 Schematic diagram of the Mn12 exchange interactions. The S_4 symmetry axis c is perpendicular to the plane through the center of the diagram. 7

2.3 The double well potential for Mn12-AC (a) when $B_z = 0$, the potential is symmetric and the states M and $-M$ are degenerate. (b) At resonance $N = 1$ when $M = -10$ and $M = 9$ are degenerate. Note that other states which satisfy $M + M' = \pm 1$ are slightly off resonance due to the presence of the quadratic term AS_z^4 in the Hamiltonian. 8

2.4 The six isomers resulted from the acetic acids distortions. The reduced symmetry groups are shown below each of the isomers. Figure taken from reference [23]. 16

2.5 Two inequivalent anisotropy parameters are due to the two different octahedral environment surrounding them. Figure taken from reference [32] 18

2.6 4 possible coordinations of acetic acids for the isomer $n = 2$ "cis" (see figure 2.4). 18

2.7 Level anticrossing arising from introducing off diagonal elements that mix states $|0\rangle$ and $|1\rangle$ at the point were the gap between them is minimum. 20

2.8 4-fold symmetry pattern in tunneling rate in the hard-medium plane of the Mn12-AC crystal. Figure is taken from reference [30]. The index k in this figure is the same as the parameter N used throughout this thesis. 21

2.9 2-fold symmetry in the tunneling rate. Figure taken from reference[30]. 22

3.1 NMR signals observed for the Mn12-AC oriented powder at zero applied field and $T = 1.5$ K. Three distinguished lines are due to three inequivalent types of Mn ions. 26

3.2 The peak frequency dependence on longitudinal magnetic field for the three types of Mn ions in the Mn12-AC molecule. The slopes are shown to be in agreement with the gyromagnetic ratio of the ^{55}Mn nucleus, $\gamma_N/2\pi = 10.5$ MHz. Figure is taken from reference [33] 27

3.3 ^{55}Mn NMR spectra at $H = 1.2$ T after zero-field cooling to 1.4 K (off-equilibrium state). The inset shows the field dependence of the resonance frequency for each split peak. Figure taken from reference [33]. 28

3.4 NMR frequencies of the three Mn ion types versus external transverse magnetic field. Solid lines are theoretical calculations assuming single spin model. Figure taken from reference [12]. . . . 29

3.5 Schematic view of the canting effect due to presence of transverse field H_x. The hyperfine field shows is the one created by the Mn^{4+} at their nuclear site. The Hyperfine of the Mn^{3+} has an apposite direction of the one shown in this figure leading to the different dependence on magnetic field shown on figure 3.4. 30

3.6 The nuclear coordinate system (ξ, η, ζ) where the nuclear Zeeman is taken in the direction of the total magnetic field. 32

3.7 The splitting of the ground state in Kelvins and Larmor frequency as a function of transverse magnetic field. Resonance is expected at $H_\perp \approx 5.35$ T. 34

3.8 Two possible canting schemes due to the two ground state spin directions. Longitudinal components of the field **H** can lead to two different frequencies corresponding to two different vector sum of the fields. 40

3.9 (right) Energy spectrum of the Hamiltonian 3.4 vs. longitudinal (top right) and perpendicular(bottom right) applied field. (left) the corresponding reciprocal of energy levels' lifetimes due to spin-phonon interaction calculated using Eq. 3.11. Inset of bottom right figure shows the effect of introducing a small longitudinal field on the tunneling splitting of the ground state. 41

3.10 $1/T_1$ dependence on applied field, both perpendicular and parallel to the molecule's easy axis c. Dashed lines show the effect of misalignment of the clusters easy axis to the applied field. Inset shows the low field portion of the $1/T_1$ dependence on applied transverse field for different values of internal transverse fields. Experimental data or obtained via private communications with Y. Furukawa. 42

4.1 The Spin model proposed for the Mn12-AC molecule under the assumption $J_1 \gg J_2$, J_3 and J_4. 45

4.2 Dependence of the tunneling splittings $\Delta E_{\pm M}$ (in kelvin) versus the number of levels taken into account in the many-spin calculations. The parameter set **A** (see text) has been used for calculations. The results for $M = 8$, 6, 4, and 2 are presented. tunneling splittings for the levels with odd M are zero because of the symmetry properties of the spin Hamiltonian. 55

5.1 Sketch of the arrangement of the manganese and oxygen ions in the inner cubane of Mn12-AC molecule. Arrows show the directions of the displacement of the Mn^{4+} ions which lead to the formation of the inner cubane instead of the perfect cube. Figure and caption are taken from Ref. [63]. 60

5.2 Lowest energy levels of Eq. (5.2) within each of the $S_z = 0, \pm1, \pm2, ..., \pm10$ blocks resulting from using sets 4 (top) and 5 (bottom) and including single ion anisotropies from table 5.3. Some levels are annotated by their expectation value of S to show the degree of spin state mixing. The α lines show low energy expected transitions from the ground state as allowed by selection rules in the neutron scattering experiment. The lowest manifolds $S = 10$ and $S = 9$ spectrum were fit for the anisotropy Hamiltonian $-DS_z^2 - AS_z^4$ and the parameter values of the fit are shown in the boxes. . . . 68

5.3 Higher scale of energy levels of Eq. 5.2 within each of the $S_z = 0, \pm1, \pm2, ..., \pm10$ blocks resulting from using sets 4 (top) and 5 (bottom) and including single ion anisotropies from table 5.3. The α lines show some of the expected transitions from the ground state as allowed by selection rules in the neutron scattering experiment. 69

5.4 71

Chapter1 Introduction

The topic of Molecular Magnets has grown in the last decade due to the fact that these magnets have shown a coexistence of classical and quantum behaviours in magnetic properties and for the fact that the magnetic building blocks, magnetic clusters, lie on the frontier between the microscopic and the macroscopic scales. Each of these magnetic clusters consists of number of transition metal or rare earth ions (quantum spins) which are exchange coupled, making the cluster act like a single macroscopic classical spin at low temperatures and isolated from ions from neighbouring clusters by organic groups surrounding them. The sense of using a classical description comes from behaviour in which, for example, at low temperatures, molecular magnets show magnetic hysteresis in relaxation experiments. At the same time, these hysteresis loops at low temperature show jumps of their magnetic moment at regularly spaced magnetic fields, an indication of quantum tunneling of magnetization (QTM) [1, 2, 3] as shown in figure 1.1. This duality in behaviour indicates that these molecules lie in the crossing line between the microscopic and macroscopic worlds. The line, which is often referred to by the term *mesoscopic* scale, lies in the region ranging from the sub-nanometer to few nanometers in size. Unlike in bulk magnets, the hysteresis loops, as well as the other magnetic properties, of molecule-based magnets are purely from molecular origin, for which they often called *single-molecular magnets* (SMMs). The hysteresis loops and the slow relaxation shown by these molecules are the essential elements which make these magnets candidates for the next generation of small size magnetic storage media [4].

Exchange interactions among the ions of the molecule, which are often antiferromag-

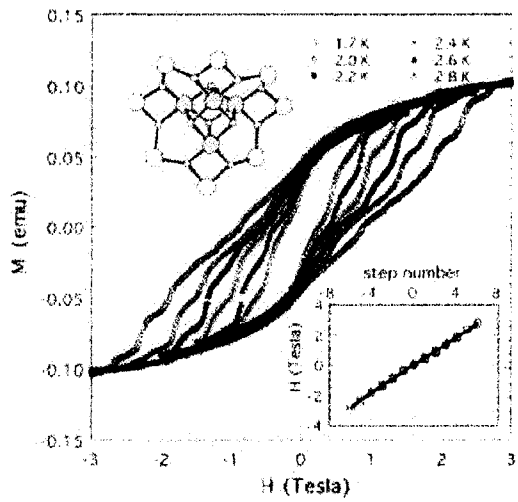

Figure 1.1 Hysteresis loops at low temperatures show sudden jumps of magnetization at regularly spaced intervals (see inset) of the applied magnetic field. Figure is cited from [1].

netic, sometimes lead to a ground state with a large magnetic moment. With this large moment, a moderate value of anisotropy parameter creates a large anisotropy barrier between equally preferred opposite orientations of the magnetic moment (along and opposite to the easy axis created by the anisotropy), which can explain the hysteresis and slow relaxation. The large anisotropy of the molecules separates the lowest states in each side of the barrier by an energy gap of several Kelvins, a criterion considered to be a necessary ingredient in a good candidate for *quantum bits* [5], the counterpart in *quantum computing* to the binary digit or bit in classical computing.

The observed jumps of the magnetization of magnetic molecules as a function of applied magnetic field demonstrates the quantum nature of these systems. The fact that magnetic molecules consist of several interacting moments constitutes a challenging theoretical problem to understand the global magnetic response of the molecule in terms of its constituent ion moments. Since the discovery of this class of material, very little work has considered the multi-spin nature of the molecules. Rather, they are often

considered as a rigid spin of value equal to the spin of the ground state, where states of high energies are conveniently ignored. Such an approach reduces the size of the problem considerably and can successfully explain the locations of energy states within each side of the anisotropy barrier. From such simplified models, for example, one can estimate the thermal relaxation times (not those associated with the jumps in hysteresis loops), and the anisotropy barrier size responsible for hysteresis. On the other hand, the single-spin model can not fully explain magnetic properties involving excited states of high energies such as those proposed by inelastic neutron scattering experiments. It also fails to quantitatively explain the phenomena of spin tunneling responsible for the jumps of magnetic moment observed in hysteresis loops.

In chapter (2), we will review the single spin model proposed for one of the most studied magnetic molecules, Mn12-AC. In chapter (3), we will apply this model to explain and understand the nuclear magnetic relaxation of the Mn nucleus in response to applied field.

In chapter (4), we will present the first attempt of understanding the tunneling phenomena of the Mn12-AC magnetic molecule taking into account its multi-spin nature. We show that simplification schemes based on excluding higher energy states of the molecule, assumed to be irrelevant, yield unreliable results. In Chapter (5), we present investigations looking into the problem of magnetic molecules using the complete picture of interacting ions. The first step toward full understanding of the multi-spin nature of Mn12-AC is by exploring the magnetic exchange interaction between the ions of the molecule and by examining the contribution of anisotropy of each individual ion. Our quantum mechanics formulation is based on matrix representation of interactions. The fact that magnetic interactions, such as exchanges, yield extremely sparse matrices[1], makes the problem of magnetic molecules more feasible using modern advancements of nowadays computers and algorithms.

[1] A matrix is called *sparse* when it contains a small percentage of non-zero elements.

Chapter2 Single-spin Model Of The Molecule Mn12-AC

An aspect of molecular magnets that makes them ideal candidates for the study of QTM is that they are composed of identical magnetic subunits which have chemically well determined properties. A reasonable sample size (say sub mm^3) prepared for measurements would consist of around $\sim 10^{17} - 10^{18}$ magnetic clusters with the same magnetic properties and characteristic energies. Another aspect of these magnets relates to their spin value in the ground state, which is of the order of $S \sim 10$. While this spin is somewhat large for a molecular system, it is small relative to most superparamagnetic systems. This value leads to to appreciable energy separation of the spin levels for moderate values of crystalline anisotropies. As a result, a large energy barrier (tens of kelvins) exists that separates opposite spin projections along the direction of anisotropy axis. As we will see later in this chapter, this very barrier is responsible for the observation of both the classical hysteresis and the quantum tunnelling of the magnetic moment.

For spin systems of relatively high spin values S, we can express the spin Hamiltonian as a linear combination of the *Stevens operators* [6, 7] O_k^q in the form $\sum_{q,k} B_k^q O_k^q (S_x, S_y, S_z)$ where $S^2 = S_x^2 + S_y^2 + S_z^2$. Without going into the details of these operators, they simply result in a power series of spin projections as follows:

$$\mathcal{H} = DS_z^2 + AS_z^4 + E_1 \left(S_x^2 - S_y^2\right) + C \left(S_+^4 + S_-^4\right) + \cdots, \tag{2.1}$$

where D, E, and C are referred to as anisotropy parameters, $S_\pm$: $S_\pm = S_x \pm iS_y$ are

the spin raising (lowering) operators, and S_z is the spin projection along the quantum axis that usually is chosen conveniently as the easy axis of the molecule. That is, the direction along which the spin minimizes its energy.

The well characterized arrangement of the magnetic (and as well the non magnetic) atoms within each of the clusters, enables us to identify the crystalline geometry and identify the crystalline anisotropy axes. Furthermore, symmetries imposed by the crystal structure allow us to predict which terms in Eq. (2.1) vanish and which terms survive, as we will discuss below for the Mn12-AC case.

2.1 Overview of Mn12-AC magnetic molecule

The magnetic molecule $[Mn_{12}O_{12}\,(CH_3COO)_{16}\,(H_2O)_4]\cdot 2\,(CH_3COOH)\cdot 4\,(H_2O)$ (or Mn12-AC for abbreviation) was first synthesized by Lis [8] in 1980 but has gained much interest after it was discovered that the compound had a ground state of a high value of $S = 10$ using AC susceptibility measurements [9, 10] in the early 1990's. The Mn12-AC cluster contains four Mn^{4+} ($S = 3/2$) ions forming a central tetrahedron surrounded by eight Mn^{3+} ($S = 2$) ions in a non-planar ring as shown in figure 2.1. Each of the Mn^{4+} ions, shown in figure 2.1 in green, is coupled to the nearest three Mn^{3+} ions, shown in figure 2.1 in orange, via strong antiferromagnetic exchanges through oxygen bridges, while same valence ions are coupled via considerably weaker antiferromagnetic (or possible ferromagnetic) exchanges with their nearest neighbours (see table 2.1 for the Mn-Mn distances within the molecule). In effect, this exchange competition, should lead to an aligned Mn^{4+} antiparallel to the Mn^{3+} ions as illustrated in the schematic figure 2.2. This configuration has been confirmed experimentally by polarized neutron diffraction studies [11] and ^{55}Mn NMR measurements [12]. The resultant spin of such configuration is $S = 8\times 2 - 4\times 3/2 = 10$. The magnetic core is surrounded by 16 acetate ions and 4 water molecules per cluster. The nonmagnetic ligands isolate the cluster

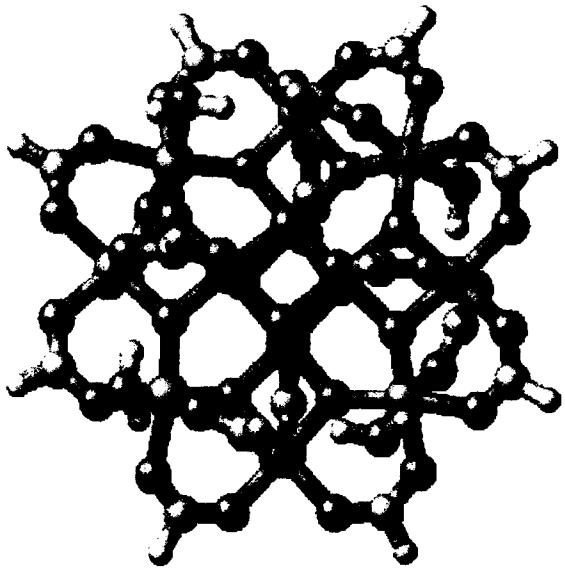

Figure 2.1 The magnetic Molecule Mn12-AC viewed slightly off symmetry axis c. In this figure only the Mn, Oxygen and Carbon ions are shown. Hydrogens were omitted for simplicity.

from its neighbours so that they interact only via dipolar fields which are considered negligible compared to the exchange parameters, since different clusters are separated by distances > 7 Å and because the Curie-Weiss temperature is < 70 mK [13, 14, 15, 16]. As a result of cluster isolation from neighbouring clusters, the Mn12-AC magnetic molecule is considered to belong to the family of Single-Molecule Magnets (SMMs) which behave as superparamagnetic particles with no long range order and where the system can be described, at least for low temperature regimes, by a Hamiltonian of an uncoupled single spin, as in Eq. (2.1).

Table 2.1 Mn-Mn distances for the different exchange couplings in Mn12-AC.

exchange path	J_1	J_2	J_2'	J_3	J_3'	J_4	J_4'
Mn-Mn distance (Å)	2.77	3.45	3.46	2.82	2.94	3.33	3.41

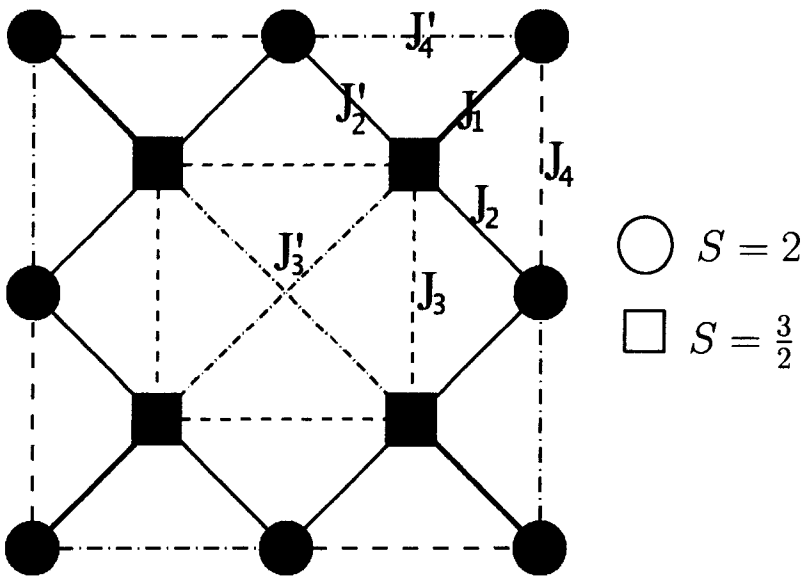

Figure 2.2 Schematic diagram of the Mn12 exchange interactions. The S_4 symmetry axis c is perpendicular to the plane through the center of the diagram.

As one can deduce from the figures 2.1 and the diagram in figure 2.2, if we assume no dislocation of Mn ions due to distortions within the crystal, Mn12-AC has tetragonal structure associated with the S_4 symmetry group.[1] The c axis is the smallest lattice parameter and is perpendicular to the plane shown in figures 2.1 and 2.2 passing through the center of the molecule [8]. This axis will be denoted as the anisotropy easy axis of the crystal. According to such symmetry, the $x-$ and $y-$axes are indistinguishable, leading to the assumption that the transverse anisotropy parameter $E_1 = 0$. The lowest-order transverse term allowed by S_4 is the fourth order term appearing in Eq. (2.1). This fourth order term allows transitions between spin states M and M' only if $M - M'$ is a multiple of ± 4 as will be explained later in section 2.5. This is an interesting feature related to spin systems. The terms in the Hamiltonian allow us to associate magnetic properties with certain spin states because of this selection rule. Before we

[1] Actually, Mn12-AC was found to have symmetry lower than tetragonal due to disorder. We will discuss this in section 2.4 on page 14.

$$E = DM^2 + AM^4 - 1.33MB_z,$$
$$D = -0.55\,\text{K and}\,A = -1.2\,\text{mK}.$$

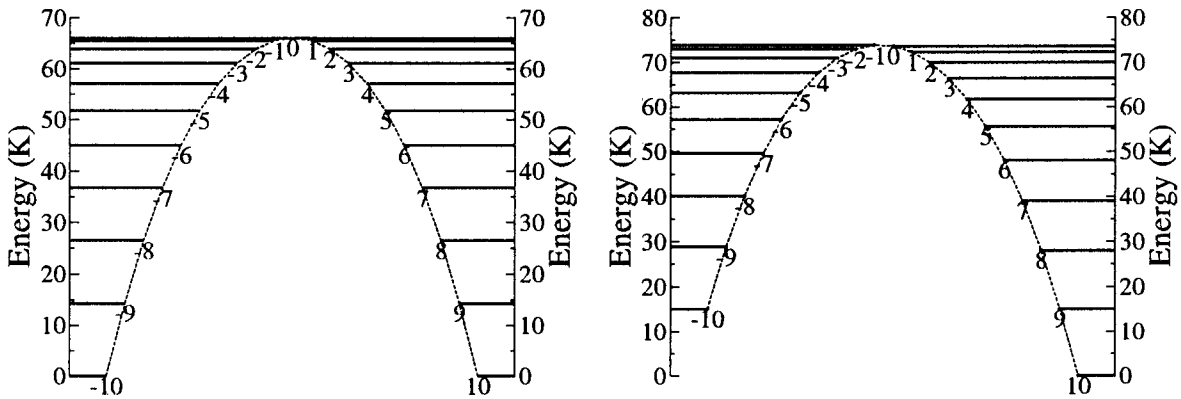

(a) $B_z = 0$ (b) $B_z = 0.577$ T

Figure 2.3 The double well potential for Mn12-AC (a) when $B_z = 0$, the potential is symmetric and the states M and $-M$ are degenerate. (b) At resonance $N = 1$ when $M = -10$ and $M = 9$ are degenerate. Note that other states which satisfy $M + M' = \pm 1$ are slightly off resonance due to the presence of the quadratic term AS_z^4 in the Hamiltonian.

discuss selection rules obeyed by the Mn12-AC system, we shall review the properties of the Hamiltonian in Eq. (2.1) for the values of anisotropy parameters known for the Mn12-AC magnetic molecule.

2.2 Double-well energy potential

From various techniques such as inelastic neutron scattering (INS) [17, 18] and electron paramagnetic resonances (EPR) [19] on oriented powder of Mn12-AC, anisotropy parameters appearing in the Hamiltonian in Eq. (2.1) were determined to have the values $D \sim -0.55$ K and $A \sim -1.2$ mK. Transverse terms appearing in Eq. (2.1) introduce very small shifts to the energy levels, hence they can be neglected in the zeroth order and treated as a perturbation. Since the first two terms in the Hamiltonian $\mathcal{H}$ are

negative, the cluster becomes *bistable*, in the meaning that the system, in the absence of applied field, has two equally preferred directions, associated with spin up and spin down. Since both D and A are negative, states of lowest energies are the ones which have spin projection value $M = \pm 10$, while the state $M = 0$ has the highest energy. The Hamiltonian, in other words, has the form of a double well potential with each of the states $M = \pm 10$ at the bottom of each well and separated by energy barrier of height $\Delta = -10^2 D - 10^4 A \sim 67$ K centered at the state $M = 0$. A schematic diagram of the double-well potential is shown in figure 2.3a at zero applied field. We can see that $\pm M$ levels from both sides of the barrier are degenerate. This degeneracy will be called the $N = 0$ level crossing where $N \equiv M + M'$. As one applies a magnetic field B_z along the easy axis of the molecule, the system acquires an energy term of the form $-\hbar\gamma_e M B_z$. Energy of the states with spin projections parallel to the magnetic field ($MB_z > 0$) will decrease, while the ones antiparallel to the field will increase. We can increase the applied field until the next set of level crossings come into the picture, namely between the states M and $M' = -M + 1$ (see figure 2.3b), which we will refer to as the $N = 1$ level crossing. Note, however, that because of the fourth order anisotropy term, AS_z^4, the states do not resonate simultaneously as in the case of $N = 0$ level crossing, but rather, come one after another in very small magnetic field intervals that can be calculated by knowing the values of D and A [20]. The magnetic field can be raised further until the $N = 2$ set of level crossings, and again a family of close resonances appear for equal energy states M and $M' = -M + 2$. Continuing raising the field, we will come across all resonances until we reach $N = 19$[2] corresponding to $M = -10\,(10)$ and $M' = -9\,(9)$. The question is: at which of these level crossings spin tunneling should take place and at which of these level crossings spin tunneling is observed.

[2]Practically, there is a maximum value of N, less than the theoretical value $N = 19$, that can be experimentally observed, when the applied magnetic field, B_z, lowers the potential barrier to a point where relaxation by jumping over the barrier (thermal relaxation) becomes faster than relaxation through tunneling.

2.3 Quantum tunneling of magnetism and selection rules in Mn12-AC

Quantum Tunneling is a phenomena in which the system changes its state by passing through a classically forbidden region. Before we attempt to understand what this implies, let us think of the spin of the molecule as a classical vector pointing, say, toward the positive $z-$axis (corresponding to the $M = 10$ state in the quantum picture). The only way for that vector to reverse its direction is by rotating so that θ (defined as the angle between the spin and the positive $z-$axis) changes continuously from 0 to π. Since $\theta = \pi/2$ is a point which corresponds to a maximum of the potential[3] (when $B_z = 0$), the spin simply can not reverse direction without an external force large enough to provide the molecule an amount of energy of, at least, the value of the barrier height. Quantum mechanically, on the other hand, the Mn12-AC molecule tunnels from one well to the other at any level crossing (provided it is allowed by selection rules) without climbing the barrier. At the $N = 0$ level crossing, for instance, the molecule can flip its spin from M to $-M$ without passing through any of the intermediate states M': $|M'| < |M|$.

Since we are going to treat the fourth order term in Eq. (2.1) (and, in fact, all other terms which include off-diagonal elements in the S_z basis) as a perturbation, it is convenient to gather terms which commute with S_z in one Hamiltonian operator, $\mathcal{H}_0$:

$$\mathcal{H}_0 = DS_z^2 + AS_z^4 - \hbar\gamma_e B_z S_z, \tag{2.2}$$

while all other terms which do not commute with S_z are absorbed in the perturbation

[3]Classically, the energy of the spin due to the anisotropy potential is $E = -D\,M^2 - A\,M^4$ where $M = S\cos\theta$. If $D > A > 0$, $\frac{dE}{d\theta} = 0 \Rightarrow \theta = 0, \pi$ (corresponding to minima) and $\theta = \pi/2$ (corresponding to a maximum).

$\mathcal{H}'$:

$$\mathcal{H}' = \mathcal{H}_T^{(1)} + \mathcal{H}^{(2)} + \mathcal{H}^{(4)} + \cdots \tag{2.3}$$

$$\mathcal{H}_T^{(1)} = -\hbar\gamma_e \left(B_x S_x + B_y S_y\right) \tag{2.4}$$

$$\mathcal{H}^{(2)} = E_1 \left(S_x^2 - S_y^2\right) + E_2 \left\{S_x, S_y\right\} = \frac{E_-}{2} S_+^2 + \frac{E_+}{2} S_-^2 \tag{2.5}$$

$$\mathcal{H}^{(4)} = C \left(S_+^4 + S_-^4\right), \tag{2.6}$$

where $E_\pm = E_1 \pm i\, E_2$ and $\left\{\hat{A}, \hat{B}\right\} = \hat{A}\hat{B} + \hat{B}\hat{A}$ is the usual anticommutation relation. Note that we have included the term $\mathcal{H}^{(2)}$ in the definition of $\mathcal{H}'$ although we argued that Mn12-AC molecule shall not have such term in the Hamiltonian. We justify it since the majority of the Mn12-AC molecules have lower symmetry than S_4 as suggested in reference [23] and will be discussed in section 2.4.

Assume that a spin is initially at a state $|\psi\,(t=0)\rangle$. At later time t, according to the Schrödinger's picture, the system will be in the state $|\psi\,(t)\rangle$ such that

$$|\psi\,(t)\rangle = e^{-it\mathcal{H}/\hbar} |\psi\,(0)\rangle, \tag{2.7}$$

where

$$\mathcal{H} = \mathcal{H}_0 + \mathcal{H}'. \tag{2.8}$$

Now let us assume that perturbation is turned off, $\mathcal{H}' = 0$. If the system is initially at state $|M\rangle$, then the probability of the state to be in state $|M'\rangle$ at later time t is $|\langle M'|\psi\,(t)\rangle|^2 = \left|\langle M'|\, e^{-i\mathcal{H}_0 t/\hbar}\, |M\rangle\right|^2 = \left|e^{-iE_m t/\hbar}\, \langle M'|M\rangle\right|^2 = \delta_{M.M'}$. That is, the molecule stays at the state $|M\rangle$ forever. This simply means that the expectation value of S_z will not change in time as one can, using the Heisenberg picture, check easily with the time evolution of the operator S_z: $\langle\psi|\, S_z\,(t)\, |\psi\rangle = \langle\psi|\, e^{i\mathcal{H}_0 t/\hbar} S_z e^{-i\mathcal{H}_0 t/\hbar}\, |\psi\rangle = \langle\psi|\, S_z\, |\psi\rangle$ where

we used the lemma [24]:

$$\begin{aligned} e^{\lambda A} B e^{-\lambda A} &= B + \frac{\lambda}{1!}[A,B] + \frac{\lambda^2}{2!}[A,[A,B]] + \frac{\lambda^3}{3!}[A,[A,[A,B]]] + \cdots \\ &\equiv \sum_{k=0}^{\infty} \frac{\lambda^k}{k!} A^k \{B\}, \end{aligned} \tag{2.9}$$

and the fact that $[S_z, \mathcal{H}_0] = 0$. Note that we omitted the time dependence of ψ because in the Heisenberg picture, states are stationary and time dependence is transferred to operators.

If perturbation is turned on, on the other hand, the system prepared initially to be the state $|\psi(t=0)\rangle = |M\rangle$ will have a probability to be in other states $|M'\rangle \neq |M\rangle$ at later time t which can be computed as follows:

$$|\langle M'|\psi(t)\rangle|^2 = \left|\langle M'| e^{-i(\mathcal{H}_0+\mathcal{H}')t/\hbar} |M\rangle\right|^2. \tag{2.10}$$

Since $|m\rangle$ is not an eigenstate of the total Hamiltonian $\mathcal{H} = \mathcal{H}_0 + \mathcal{H}'$, one needs to expand the exponential function in the last equation as a power series in order to be able to apply the Hamiltonian operator on $|M\rangle$ as follows:

$$\langle M'| e^{-i(\mathcal{H}_0+\mathcal{H}')t/\hbar} |M\rangle = \sum_{k=0}^{\infty} \left(\frac{-i\,t}{\hbar}\right)^k \frac{\langle M'| (\mathcal{H}_0 + \mathcal{H}')^k |M\rangle}{k!}. \tag{2.11}$$

Following the series in the last equation to higher orders is tedious work. However, it gives an insight on how selection rules can be invoked by knowing the perturbation $\mathcal{H}'$. Assume that only $C \neq 0$ and both $\mathcal{H}^{(1)}$ and $\mathcal{H}^{(2)}$ are zero, so $\mathcal{H}' = \mathcal{H}^{(4)}$. Off diagonal operators $S_\pm$ in $\mathcal{H}^{(4)}$ will appear in the expansion terms in power multiples of four, that is, we will have

$$\langle M'| e^{-i\left(\mathcal{H}_0+\mathcal{H}^{(4)}\right)t/\hbar} |M\rangle \propto \langle M'| S_\pm^{4l} S_\mp^{4l'} |M\rangle$$

$$\propto \langle M' \pm 4l \,|M \mp 4l' \rangle$$

$$\propto \delta_{M'-M\pm 4(l'+l)},$$

where l and l' are integers. Similar treatment for the case of $\mathcal{H}^{(2)} \neq 0$ in Eq. (2.3) leads to:

$$\langle M'| e^{-i\left(\mathcal{H}_0+\mathcal{H}^{(2)}\right)t/\hbar} |M\rangle \propto \delta_{M'-M\pm 2(l'+l)}.$$

Therefore the selection rules imposed by the perturbations $\mathcal{H}^{(2)}$ and $\mathcal{H}^{(4)}$:

$$\mathcal{H}^{(2)} \Rightarrow |M - M'| = 2 \times integer, \tag{2.12}$$

$$\mathcal{H}^{(4)} \Rightarrow |M - M'| = 4 \times integer, \tag{2.13}$$

mean that spin tunneling will be observed only at every other fourth level crossing when only $\mathcal{H}^{(4)}$ is present in the perturbation in Eq. (2.3), while only tunneling at every other level crossings will be observed in the case of only $\mathcal{H}^{(2)}$ is present.

In the relaxation experiments on Mn12-AC crystals [1, 2, 3, 20], tunneling was observed at all level crossings and selection rules (at least those outlined earlier) do not appear to be followed by the molecule. This means that terms of the Hamiltonian that mix states M with $M \pm 1$ are essential in explaining $N =$ odd level crossings in the data obtained in such experiments. Such terms can result from either intrinsic fields acting on the molecules (come from nuclear hyperfine fields and inter-molecular interactions such as dipole and exchange) leading to a non-vanishing perturbation term $\mathcal{H}_T^{(1)}$ in Eq. (2.3), or from other terms such as:

$$\mathcal{H}_A^{(1)} = G_x \{S_x, S_z\} + G_y \{S_y, S_z\}, \tag{2.14}$$

As will be discussed in section 2.4.

2.4 Lower symmetry terms in Mn12-AC

Earlier in this chapter we introduced terms in the Hamiltonian although they violate the S_4 symmetry group to which it was believed that the Mn12-AC molecule belongs as reported by Liz [8] using x-ray diffraction at room temperature. Robinson *et al.* [11, 21], on the other hand, reported a mosaic spread spread of the alignment of the crystal of $\sim 0.4^\circ$ using polarized neutron diffraction at low temperature. They attributed the disorder responsible for the mosaic to the extensive hydrogen-bonding network interaction which exists at lower temperature and slightly displaces Mn3 (Mn^{3+}) ion and its ligands. This observation was also confirmed by x-ray diffraction at low temperature by Cornia *et al.* [22]. This supports the fact that Mn12-AC has symmetry lower than tetragonal and corresponding terms in the Hamiltonian do not vanish. In this section we will discuss the possible origin of these terms and their effect on tunneling symmetry.

As we mentioned earlier, the main contributions to the crystalline anisotropy is expected to arise from the Jahn-Teller distortion of the eight Mn^{3+} ions. Magnetic anisotropy parameters of each of the Mn^{3+} ions can be calculated with great accuracy using the angular overlap model (AOM) [25, 26, 27]. The contribution of the single ion anisotropy tensors $\tilde{\mathbf{D}}_i$ to the crystalline anisotropy $\tilde{\mathbf{D}}$ in Eq. (2.17) can be estimated as follows:

$$\tilde{\mathbf{D}} = \sum_{i=1}^{8} \alpha_i \mathbf{R}_i^T \cdot \tilde{\mathbf{D}}_i \cdot \mathbf{R}_i, \tag{2.15}$$

where $\tilde{\mathbf{D}}_i$ is calculated in the crystal reference frame and $\mathbf{R}_i$ is the rotation matrix representing the symmetry operation for the i-th Mn^{3+} ion and α_i is the projection coefficient of the i-th spin whose value depends on the spin coupling scheme [28]. In

general, the anisotropy tensor is not necessarily axial or diagonal leading to a general form of the 2nd order anisotropy contribution to the Hamiltonian:

$$\mathcal{H}_A = \mathbf{S} \cdot \tilde{\mathbf{D}} \cdot \mathbf{S} \tag{2.16}$$

$$\tilde{\mathbf{D}} = \begin{pmatrix} E_1 & E_2 & G_x \\ E_2 & -E_1 & G_y \\ G_x & G_y & D \end{pmatrix}, \tag{2.17}$$

where the matrix elements in Eq. (2.17) have been introduced earlier in this chapter. E_1 creates anisotropy in the $x-y$ plane perpendicular to the easy axis along c. If $-D > E_1 > 0$, then the $x-$axis becomes the hard axis and $y-$axis becomes the medium axis and visa versa if $D < E_1 < 0$. E_2 rotates the hard and medium axes in the $x-y$ plane. Finally, $G_{x,y}$ tilt the easy axis of the molecule by an angle which can be determined by diagonalizing $\tilde{\mathbf{D}}$.

Cornia *et al.* [22, 23], proposed a model, based on detailed x-ray analysis at low temperature, in which a hydrogen-bond interactions between the disordered acetic acids and acetate ligands surrounding the Mn^{3+} ions lead to disorder of the latter. It was found that the presence of an acetic acid in a site affects the the ligands surrounding the neighbouring Mn^{3+} ions. The authors of reference [23] suggested an alternative structural model in which the acetate ligands are allowed to reside in either of two possible positions, A (when acetic acid is absent) or B (when there is an acetic acid interacting with the ligand). In average the Mn12-AC lattice comprises 4 water molecules, H_2O, and 2 acetic acid molecules, CH_3COOH, (recall the Mn12-AC formula introduced in section 2.1: $[Mn_{12}O_{12}\,(CH_3COO)_{16}\,(H_2O)_4] \cdot 2\,(CH_3COOH) \cdot 4\,(H_2O)$) per cluster not directly bounded to the core of the molecule. Since there are 4 possible sites for the acetic acid per molecule, this leads to statistically an overall 50% occupancy of the possible sites. On a local scale, a molecule can have 0, 1, 2, 3, or 4 sites occupied by acetic

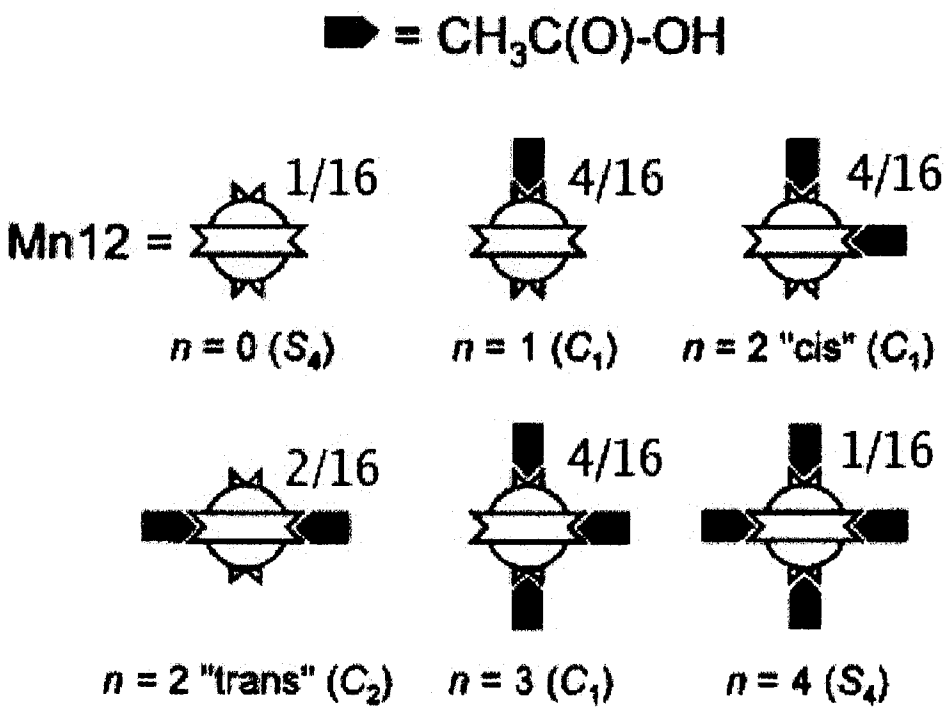

Figure 2.4 The six isomers resulted from the acetic acids distortions. The reduced symmetry groups are shown below each of the isomers. Figure taken from reference [23].

Table 2.2 Calculated Mn(II) and Mn(III) Manganese parameters corresponding to the single ion anisotropy terms: $-DS_{i,z}^2 + E\left(S_{i,x}^2 - S_{i,y}^2\right)$. δ represents the angle between the crystal's easy axis, c, and the longest axis of the octahedral environment surrounding the Mn^{3+} ions (see figure 2.5).

Site	D(K)	E(K)	δ(°)
Mn2A	4.92	0.40	11.6
Mn2B	5.27	0.27	10.7
Mn3A	4.57	0.10	37.2
Mn3B	4.40	0.07	37.1

acids giving a total of 16 possible configurations grouped into 6 types of isomers. The six isomers are shown in figure 2.4 with their relative abundance in the whole sample. Table (2.2) shows the calculated values of the 2nd order anisotropy parameters for each of the Mn^{3+} ions and the tilt angle between their easy axis and the crystalline easy axis as published in reference [23]. Note that there are two crystallographically inequivalent sites of Mn^{3+} ions (Mn2 and Mn3) due to different kinds of octahedral environment surrounding them as shown in figure 2.5. Only two of these isomers, $n = 0$ and $n = 4$, which compose only 12.5% of the magnet retain the S_4 symmetry, while the remainder isomers (87.5%) have lower symmetries. Note that for the isomer $n = 2$"cis", for example, there are four possible coordinations of the acetic acid molecules as shown in figure 2.6. The implication of this is that when a magnetic field is applied say, in the positive $x-$axis, with respect to the isomer a in figure 2.6, then it is in the negative $y-$axis with respect to the isomer b and so on for the other two.

If we calculate $\tilde{\mathbf{D}}$ in Eq. (2.17) from equation (2.16) using the parameter $\alpha_i = 0.02845$ [28] for each one of the isomers and diagonalize it, we can estimate the tilt of each isomer from the S_4 c axis. Results of this calculation are taken from Ref. [23] and listed in table 2.3. Note that misalignment due to distortion is less than 1° and the transverse parameter E_1 is in the millikelvin range, less than the easy axis anisotropy

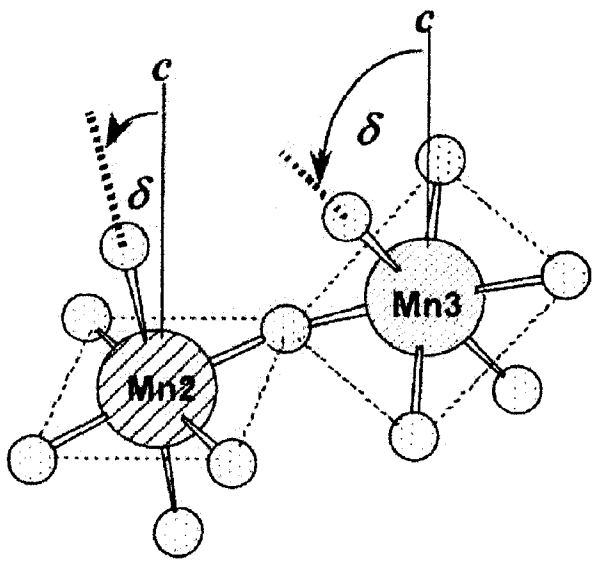

Figure 2.5 Two inequivalent anisotropy parameters are due to the two different octahedral environment surrounding them. Figure taken from reference [32]

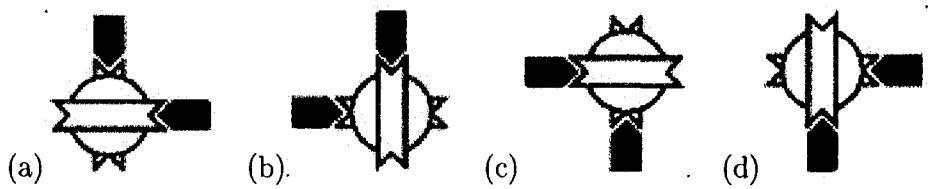

Figure 2.6 4 possible coordinations of acetic acids for the isomer $n = 2$ "cis" (see figure 2.4).

Table 2.3 Calculated magnetic anisotropy and tunnel splitting of the isomers of Mn12-AC. Table and caption are cited from Ref. [23].

isomer	concentration	D (K)	E_1 (K)	θ (°)
$n = 0$	6.25%	-0.759	0	0
$n = 4$	6.25%	-0.797	0	0
$n = 1$	25%	-0.769	2.34×10^{-3}	0.3
$n = 2$cis	25%	-0.778	1.87×10^{-4}	0.4
$n = 2$ trans	12.5%	-0.778	4.7×10^{-3}	0
$n = 3$	25%	-0.788	2.35×10^{-3}	0.3

parameter by a factor of a hundred.

2.5 Effect of different perturbation terms on tunneling properties.

Now that we have discussed the possible origin of each term of the Hamiltonian, the question is how can we verify the existence of such terms? Observation of spin tunneling can be attributed, in principle, to the presence of transverse fields originating from inter-molecular dipolar exchange and/or nuclear hyperfine interactions. Actually this statement is true since tunneling at every level crossing indeed has been observed in the magnetic molecule Mn12-BrAC (a member of the Mn12 magnetic molecule family) which strictly follows the S_4 symmetry group where terms such as in Eq. (2.14) which allows tunneling between M states differing by 1 are forbidden.

Off diagonal elements in the perturbation Hamiltonian introduces a gap (*tunnel splitting*) in the energy at what we called previously level crossings, a phenomena we shall here call a *level anticrossing* and is shown in figure 2.7. A transverse field applied along the transverse plane increases the energy gap at level *anticrossings*. By applying the transverse magnetic field along one of the medium axes, we will get a larger energy gap at the level *anticrossing* than the energy gap produced when the field is applied along

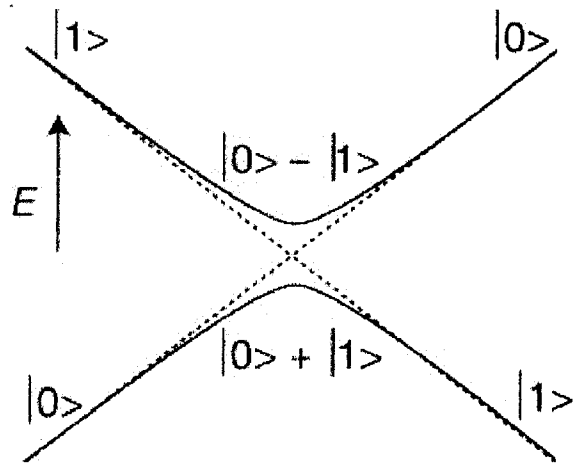

Figure 2.7 Level anticrossing arising from introducing off diagonal elements that mix states $|0\rangle$ and $|1\rangle$ at the point were the gap between them is minimum.

one of the hard axes.

By sweeping the longitudinal field so that the molecule passes through one of the level *anticrossings*, the tunneling probability of the spin can be obtained by measuring the magnetization of the sample before and after passing the level *anticrossing* and calculating the normalized change of the magnetization as follows [30]:

$$P = \frac{M_{before} - M_{after}}{M_{before} - M_{eq}}, \tag{2.18}$$

where M_{eq} as the equilibrium value of the magnetization at very high longitudinal fields. Larger tunneling splitting at level *anticrossing* leads to larger spin tunneling probability, i.e a larger change of the magnetization. If we repeat the measurement of P through one of the level *anticrossings* in the presence of a magnetic field applied at different directions (ϕ_T) on the hard-medium plane, the tunneling probability P must show a maxima at directions along the medium axis and a minimum along the hard axis. The 4−fold perturbation Hamiltonian $\mathcal{H}^{(4)}$, for example, introduces 2 hard and 2 medium

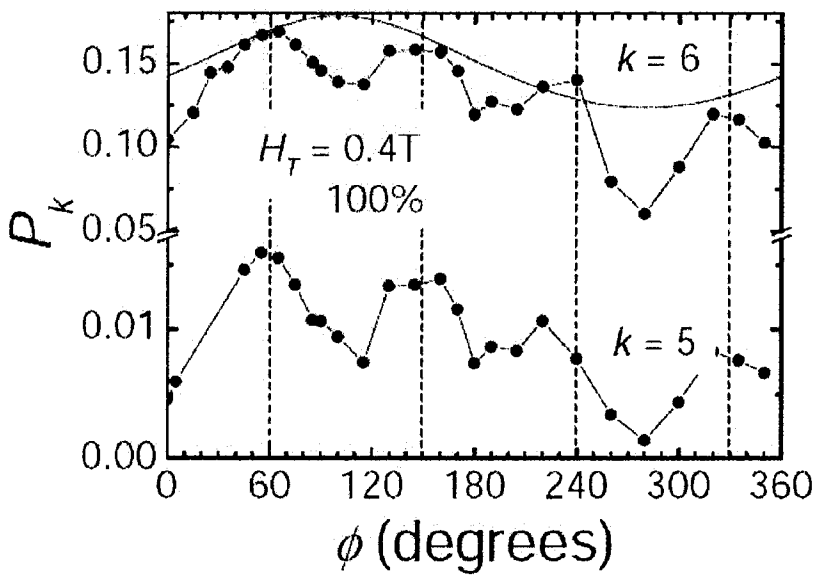

Figure 2.8 4-fold symmetry pattern in tunneling rate in the hard-medium plane of the Mn12-AC crystal. Figure is taken from reference [30]. The index k in this figure is the same as the parameter N used throughout this thesis.

axes separated by 45° in the transverse $(x - y)$ plane. Therefore, we should observe 4 minima and 4 maxima in the range $0 < \phi_T < 360°$.

Such measurements have been performed as pointed out in reference [30] and, indeed, a 4−fold pattern was observed as shown in figure 2.8 for the level *anticrossings* $N = 6$ and $N = 5$. However, the difference between maximal and minimal value of the QTM rates exhibited in this figure can not be explained by $\mathcal{H}^{(4)}$ with the known value of $C \sim 3 \times 10^{-5}$ K. The 4−fold pattern can be also attributed to a superposition of two 2−fold patterns phased by 90°. To verify this, the authors of reference [30] performed an experiment, in which they sweep the longitudinal magnetic field through a level *anticrossing* in the presence a magnetic field in the direction where the tunneling probability showed a maximum. They call this field as the selection transverse field (STF). In the presence of STF at $\phi_T = 60°$, those molecules who have their medium

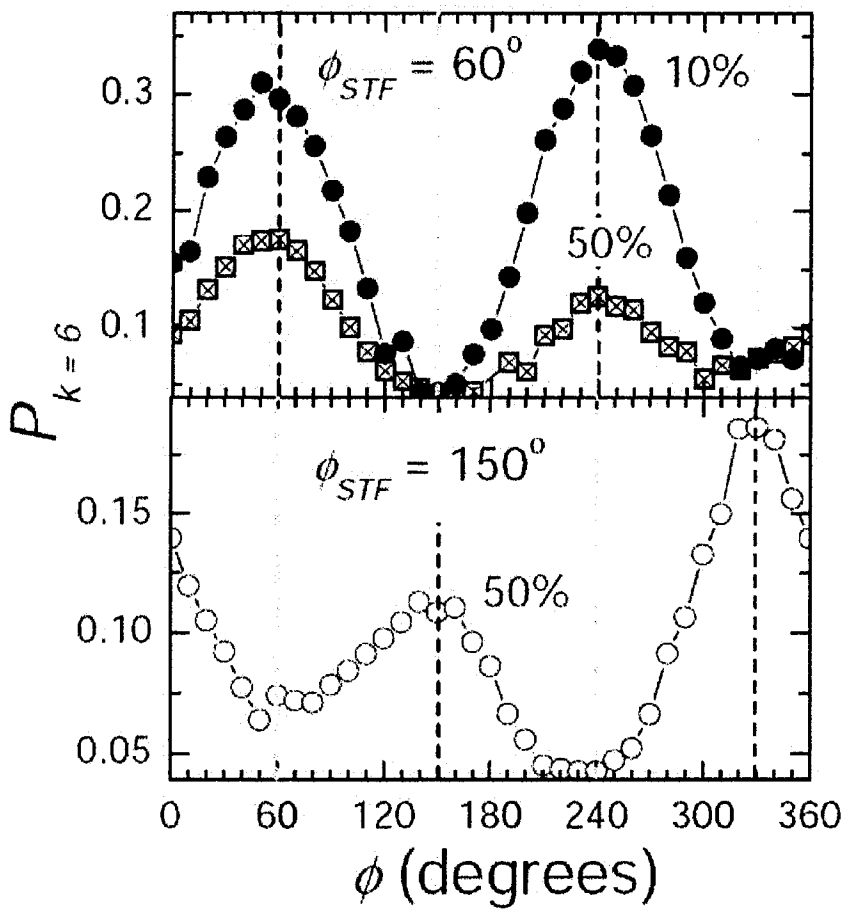

Figure 2.9 2-fold symmetry in the tunneling rate. Figure taken from reference[30].

axis in the direction of STF, will contribute the most to tunneling probability due to their larger tunneling splitting. This leads to a sample in which most of the molecules who have their medium axis along the STF are in one well of the potential energy while molecules who have their medium axis 90° from the STF, are in the other potential well. These molecules can be used for further tunneling symmetry measurements. As shown in figure 2.9, each subset of the molecules (for two cases of subset selections, total 10% and 50% of the molecules) shows a 2−fold pattern confirming the existence of a 2nd order anisotropy terms $E_1 \neq 0$.

Two other points one can draw from figures 2.8 and 2.9. There is a 1−fold pattern contribution to the QTM probability. Such pattern can arise when $G_{1,2} \neq 0$ in Eq. (2.17). The second point can be drawn by noting the the maxima of the tunneling probability are at $\phi_T = 60^\circ$ and not at $(2k+1)\frac{\pi}{4}$, where k=*integer*, as the terms $\mathcal{H}^{(4)}$ and/or $E_1\left(S_x^2 - S_y^2\right)$ would suggest. A confirmation of the conclusion drawn earlier that the 4−fold tunneling pattern is not due to $\mathcal{H}^{(4)}$ and that E_2 appearing in Eq. (2.17) is not zero.

In conclusion, the overall S_4 symmetry of the Mn12-AC magnetic molecule is distorted locally by the presence of the interaction between the acetic acids and the acetate ligands surrounding the Mn^{3+}. This introduces terms in the Hamiltonian that can assist the local fluctuating internal fields in the phenomena of magnetic quantum tunneling that can not be explained otherwise by the existence of fourth order anisotropy only.

Chapter3 ^{55}Mn Magnetic relaxation in Mn12-AC

In this chapter, we will study the mechanism of the thermal relaxation of the ^{55}Mn nuclear spin in relation to the nuclear magnetic resonance experiment on the magnetic molecule Mn12-AC. The predominant mechanism is provided by the fluctuation of local magnetic field at the nucleus site coming from the fluctuating electronic spins. T. Moriya [31] developed a theory to study such mechanism for the case of antiferromagnetic (AFM) solids where local fields at the nucleus (^{1}H nuclei) site under question is due to long range dipole interactions with lattice spins. In the magnetic molecule Mn12-AC, on the other hand, the local field at the ^{55}Mn nucleus is mainly coming from its local ion spin and all long range interactions with other ions in the crystal are negligible. At low temperature, when the ground state life time is very long in the nuclear relaxation time scale, the local field is not proportional to the thermal average of the electronic spin. We will take into account this difference between the case of the Mn12-AC magnetic molecule and the AFM case investigated by T. Moriya. Furthermore, at the end of this chapter we will comment on the fact that Mn12-AC crystals are composed of different isomers (discussed in chapter 2) and how this affect the analysis presented in this chapter.

The hyperfine interaction between the i-th Mn ion in the Mn12-AC cluster and its nuclear spin takes the form:

$$\mathcal{H}_{hf} = -\mathbf{S}_i \cdot \tilde{\mathbf{A}}_{hf} \cdot \mathbf{I}_i. \tag{3.1}$$

The Hyperfine coupling tensor $\tilde{A}_{hf}$ is diagonal (Fermi type) for the Mn^{4+} ion ($3d^3$,^{4} F) which is orbital singlet ground state. On the other hand, the ground state of the Mn^{3+} ion ($3d^4$,^{5} D) is a doublet with its two levels additionally split by the Jahn-Teller distortion and admixed by the orthorhombic distortion of the crystalline field leading to non-vanishing off diagonal elements in $\tilde{A}_{hf}$ [32]. The hyperfine tensor was calculated for each of the three Mn ion types in reference [32] to be as follows:

$$\begin{aligned}
\mathbf{A}_{hf}^{(1)} &= \begin{pmatrix} 153.5 & 0 & 0 \\ 0 & 153.5 & 0 \\ 0 & 0 & 153.5 \end{pmatrix} \text{MHz}, \\
\mathbf{A}_{hf}^{(2)} &= \begin{pmatrix} 253.9 & 0 & -24.7 \\ 0 & 176.1 & 0 \\ -24.7 & 0 & 139.7 \end{pmatrix} \text{MHz}, \\
\mathbf{A}_{hf}^{(3)} &= \begin{pmatrix} 221.0 & 0 & -53.0 \\ 0 & 180.5 & 0 \\ -53.0 & 0 & 182.2 \end{pmatrix} \text{MHz}.
\end{aligned} \tag{3.2}$$

As it can be seen in figure 3.1, the ^{55}Mn NMR signal obtained from experiments on oriented powder shows three distinct peaks at frequencies 230 MHz, 279 MHz, and 364 MHz corresponding to one of the three different types of Mn ions. These frequency lines correspond to nuclear Zeeman local fields: 21.8 T, 26.5 T, and 34.5 T, respectively. The dependence of the peak frequency on longitudinal applied field is shown in figure 3.2 for the case of a field-cooled (FC) oriented powder sample. Note that the dependence on longitudinal magnetic field is linear for all three lines with the slope in the case of the Mn^{4+} ions of an opposite sign to that of the case of Mn^{3+} ions. This means that the internal field at the ^{55}Mn nuclei coming from the Mn^{4+} ion is parallel to the applied field while the one coming from the Mn^{3+} ions is antiparallel to the applied field. Since

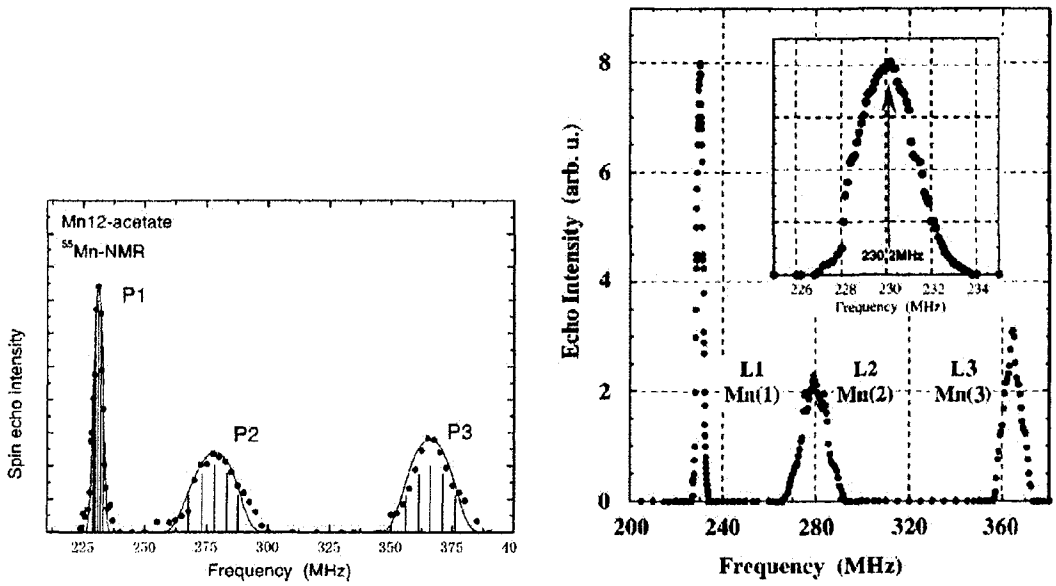

(a) From reference [33] (b) From reference [34]

Figure 3.1 NMR signals observed for the Mn12-AC oriented powder at zero applied field and $T = 1.5$ K. Three distinguished lines are due to three inequivalent types of Mn ions.

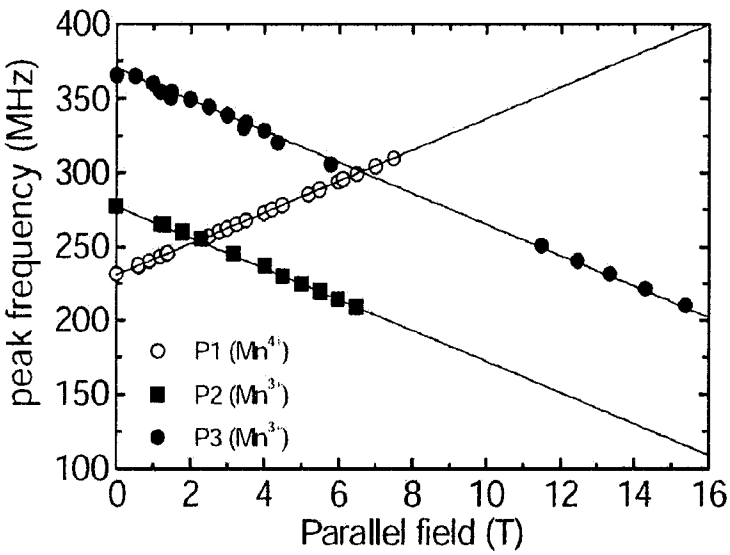

Figure 3.2 The peak frequency dependence on longitudinal magnetic field for the three types of Mn ions in the Mn12-AC molecule. The slopes are shown to be in agreement with the gyromagnetic ratio of the ^{55}Mn nucleus, $\gamma_N/2\pi = 10.5$ MHz. Figure is taken from reference [33]

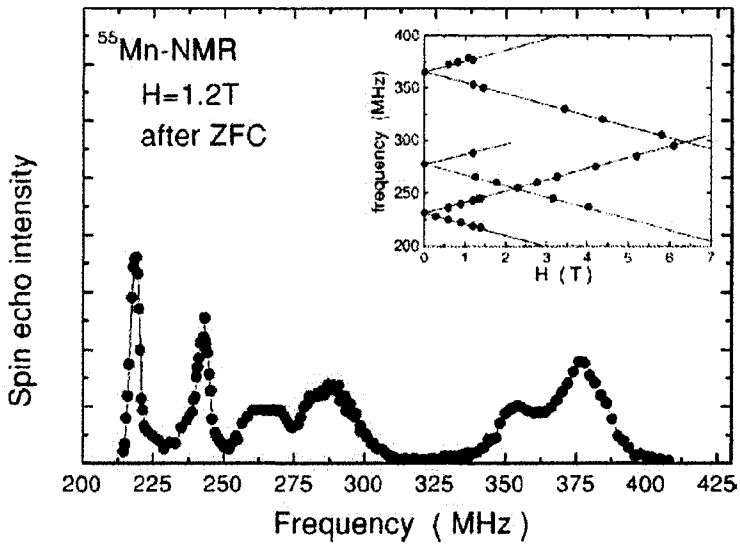

Figure 3.3 ^{55}Mn NMR spectra at $H = 1.2$ T after zero-field cooling to 1.4 K (off-equilibrium state). The inset shows the field dependence of the resonance frequency for each split peak. Figure taken from reference [33].

the direction of the magnetic field caused by the electronic spin is opposite to the spin's direction, we can conclude that the spin direction of the Mn^{3+} ions are opposite to the spin direction of the Mn^{4+}, confirming the $S = 10$ ground state picture.

The fact that we can see these signals is a clear indication that the time average of the Mn ions' spins is not zero as seen by their nuclei. These signals can be attributed to the ground state moments instead of their thermal average values. A clear indication of this is shown in figure 3.3 for a zero-field-cooled (ZFC) oriented powder sample. The spectrum was recorded at applied field $B_z = 1.2$ T in the ZFC off-equilibrium state. This means that each of the signals recorded at zero field is composed of two signals corresponding to opposite configurations of the spin moments. The inset of figure 3.3 shows the dependence of the NMR frequencies for the ZFC sample on the applied magnetic field parallel to the molecule's easy axis. Frequencies obtained at zero field split into two branches of the same slope but opposite signs, indicating that these

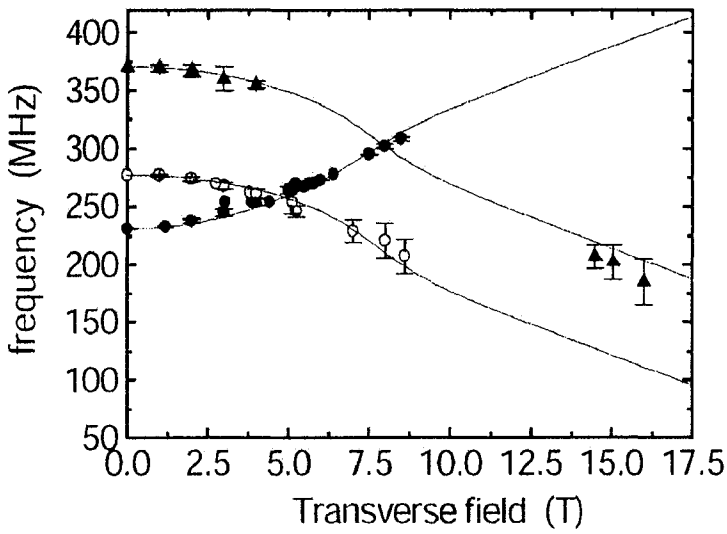

Figure 3.4 NMR frequencies of the three Mn ion types versus external transverse magnetic field. Solid lines are theoretical calculations assuming single spin model. Figure taken from reference [12].

two frequencies are due to equivalent spin configurations but opposite in direction.

Let us now consider the results of the NMR frequency recorded versus applied field perpendicular to the easy axis of the oriented powder which is shown in figure 3.4 [12]. The NMR frequency is proportional to the Zeeman field at the nucleus site which is the vector sum of the internal field and the external applied field. In response to application of a transverse field, the spins will cant in the $x - z$ plane as shown in figure 3.5. Here, the $x-$axis is simply taken along the direction of the applied filed perpendicular to the easy axis of the oriented powder. If we assume that individual spins cant rigidly in response to the external transverse field, then we can assume that the i-th spin of the cluster is proportional to the total spin and the canting angle θ_c can be calculated from the relation:

$$\sin\theta_c = \frac{M_x}{M_s}, \tag{3.3}$$

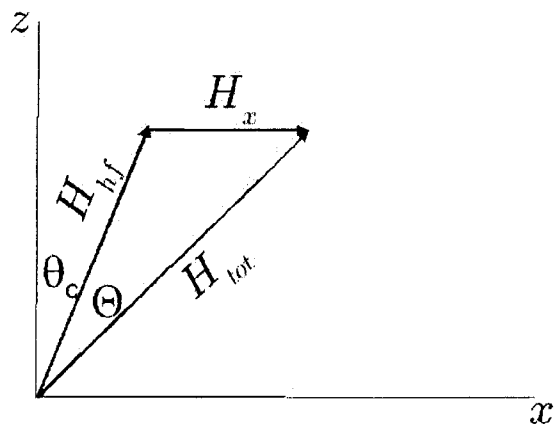

Figure 3.5 Schematic view of the canting effect due to presence of transverse field H_x. The hyperfine field shows is the one created by the Mn^{4+} at their nuclear site. The Hyperfine of the Mn^{3+} has an apposite direction of the one shown in this figure leading to the different dependence on magnetic field shown on figure 3.4.

where $M_x = \langle S_x \rangle$ and $M_s = S$ is the saturation value of the total moment in the ground state manifold. The total Zeeman field, then can be easily obtained as $H_{tot} = |\mathbf{H}_x \hat{e}_x + \mathbf{H}_{hf}|$. The agreement between the canting single spin model and experimental data is maintained for up to as high applied transverse field as 17 T as shown in figure 3.4. This justifies the use of the single spin representation of the magnetic molecule throughout this chapter in deriving the nuclear relaxation rate $1/T_1$.

3.1 Nuclear-Spin system Hamiltonian

We have seen that we could employ the same equations to calculate the field dependence of the NMR frequency for each type of the nuclei taking into account the fact that the Mn^{3+} moments are antiparallel to those of the Mn^{4+}. Therefore, throughout this section we will derive the nuclear relaxation rate $1/T_1$ of the Mn^{4+} for the simpler treatment due to the diagonal hyperfine tensor.

In presence of magnetic filed $\mathbf{H}$, the single spin Hamiltonian has the form:

$$\mathcal{H}_e = -D\,S_z^2 - A\,S_z^4 - \hbar\gamma_e \mathbf{H}\cdot\mathbf{S}, \tag{3.4}$$

where $D = 0.55$ K, $A = 1.2$ mK [17, 18, 19], and $\gamma_e = 28$ GHz/T. The total Hamiltonian that couples the i-th Mn^{4+} nuclear and electronic spins has the form $\mathcal{H}_e - A_{hf}\mathbf{I}_i\cdot\mathbf{S}_i - \hbar\gamma_N \mathbf{I}\cdot\mathbf{H}_{\text{ext}}$ where $\gamma_N = 10.5$ MHz/T and $\mathbf{H}_{\text{ext}}$ is the external applied field. We can rewrite the Hamiltonian by adding and subtracting an extra Zeeman term for the nuclear spin due to the hyperfine field introduced earlier as follows:

$$\begin{aligned}
\mathcal{H} &= \mathcal{H}_e + \mathcal{H}_N + \mathcal{H}', \\
\mathcal{H}_N &= -\hbar\gamma_N\left(\mathbf{H}_{\text{ext}} + \mathbf{H}_{hf}\right)\cdot\mathbf{I} = -\hbar\gamma_N \mathbf{H}_{\text{tot}}\cdot\mathbf{I}, \\
\mathcal{H}' &= -\alpha A_{hf}\mathbf{I}\cdot\delta\mathbf{S},
\end{aligned} \tag{3.5}$$

where $\delta\mathbf{S} = \mathbf{S} - \frac{\hbar\gamma_N}{\alpha A_{hf}}\mathbf{H}_{hf}$, and the direction of the hyperfine field $\mathbf{H}_{hf}$ is defined in figure 3.6 and its value is the same as the one obtained in zero field NMR. In Eq. (3.5), we assumed that the local spin is proportional to the total electron spin of the molecule, hence the value α is a small parameter depending on the coupling scheme of the spins in the molecule [28].

We take the projection of the nuclear spin I_ζ in the direction of $\mathbf{H} = \mathbf{H}_{\text{ext}} + \mathbf{H}_{hf}$ and define the nuclear coordinate system (ξ, η, ζ). The direction of the canting is $\hat{\mathrm{n}} = \sin\theta_c\hat{e}_x + \cos\theta_c\hat{e}_z\,(= \sin\Theta\cos\Phi\hat{e}_\xi + \sin\Theta\cos\Phi\hat{e}_\eta + \cos\Theta\hat{e}_\zeta)$ with respect to the electronic(nuclear) coordinate system (see figure 3.6). Since the quantum axis of the nuclear spin ζ does not necessarily align with the spin easy axes z, we represent the product $\mathbf{I}\cdot\delta\mathbf{S}$ in the nuclear coordinate system:

$$\mathbf{I}\cdot\delta\mathbf{S} = I_\xi\delta S_\xi + I_\eta\delta S_\eta + I_\zeta\delta S_\zeta,$$

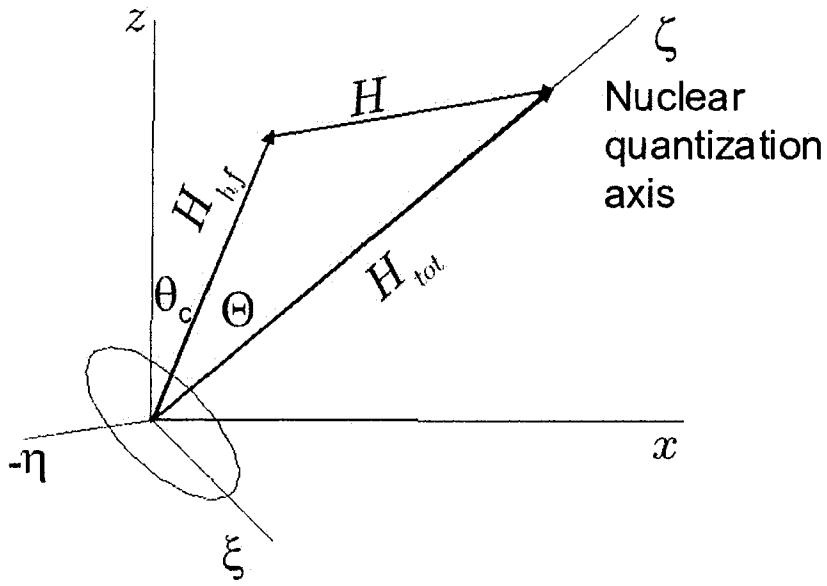

Figure 3.6 The nuclear coordinate system (ξ, η, ζ) where the nuclear Zeeman is taken in the direction of the total magnetic field.

$$= \frac{1}{2}(I_+\delta K_- + I_-\delta K_+) + I_\zeta \delta S_\zeta, \tag{3.6}$$

where $K_\pm = S_\xi \pm i\, S_\eta$ are the electronic spin ladder operators represented in the (ξ, η, ζ) coordinate system and

$$\delta K_\pm = K_\pm - \frac{\hbar\gamma_N H_{hf}}{\alpha A_{hf}} \sin\Theta e^{\pm i\Phi}. \tag{3.7}$$

We can write $K_\pm$ in terms of $S_\pm$ and S_z as follows:

$$K_\pm = e^{\mp i\Phi}\left(\pm\cos^2\frac{\theta}{2}\, S_+ \mp \sin^2\frac{\theta}{2}\, S_- - \sin\theta\, S_z\right), \tag{3.8}$$

where $\theta = \theta_c + \Theta$ as defined in figure 3.6 and Φ is the azimuthal angle in the nuclear coordinate system which can take any value in the range $[0, 2\pi]$. The nuclear Zeeman

Hamiltonian then can be expressed in a simpler way:

$$\mathcal{H}_N = -\hbar\omega I_\zeta,$$

where ω is the NMR nuclear Larmor frequency.

3.2 ^{55}Mn nuclear magnetic relaxation dependence on applied field

The transition probability from the state $|m_I, \nu\rangle$ to the state $|m_I \pm 1, \nu'\rangle$, where m_I and ν denote the nuclear and electronic states respectively, is

$$W(\nu, m_I \to \nu', m_I \pm 1) = \lim_{t\to\infty} \frac{1}{t}\frac{1}{\hbar^2}\left|\int_0^t dt' \langle m_I \pm 1, \nu'|\mathcal{H}'(t')|m_I, \nu\rangle\right|^2,$$

where

$$\mathcal{H}'(t) = e^{i(\mathcal{H}_N+\mathcal{H}_e)t/\hbar}\mathcal{H}'e^{-i(\mathcal{H}_N+\mathcal{H}_e)t/\hbar}.$$

Using these expressions in $T_1^{\pm} = (I \mp m_I)(I \pm m_I + 1)/2W(m_I \to m_I \pm 1)$ [35], we get

$$\left.\frac{1}{T_1^{\pm}}\right|_\nu = \frac{\alpha^2 A_{hf}^2}{2\hbar^2}\lim_{t\to\infty}\frac{1}{t}\left|\langle\nu'|\delta K_\mp|\nu\rangle\int_0^t dt' e^{i\frac{E_{\nu'}-E_\nu\mp\hbar\omega}{\hbar}t'}\right|^2.$$

We then evaluate the integral $\int_0^t dt' e^{ixt'} = (e^{ixt}-1)/ix \Rightarrow$

$$\lim_{t\to\infty}\frac{1}{t}\left|\int_0^t dt' e^{ixt'}\right|^2 = \lim_{t\to\infty}\frac{\sin^2\left(\frac{x}{2}t\right)}{\left(\frac{x}{2}\right)^2 t} = 2\pi\delta(x)$$

which gives us the nuclear magnetic relaxation rate due to electronic spin transition from initial state ν to final state ν' as follows:

$$\left.\frac{1}{T_1^{\pm}}\right|_{\nu} = \frac{\pi\alpha^2 A_{hf}^2}{\hbar^2}\left|\langle\nu'|\, K_{\mp}\,|\nu\rangle\right|^2 \delta\left(\frac{E_{\nu'} - E_{\nu} \mp \hbar\omega}{\hbar}\right) + 2\pi\gamma_N^2 H_{hf}^2 \delta_{\nu}(\omega)\sin^2\Theta, \tag{3.9}$$

where we employed Eq. (3.7) and averaged over possible values of Φ. Note that because of the factor $\delta\left(\frac{E_{\nu'}-E_{\nu}\mp\hbar\omega}{\hbar}\right)$ appearing in last equation, one would expect a peak in the nuclear magnetic relaxation rates at points when the Zeeman splitting of the nuclear levels matches the energy difference between the states $|\nu\rangle$ and $|\nu'\rangle$. For example, as we apply a transverse magnetic field, we create a tunneling splitting between the degenerate ground states. The dependence of such splitting on transverse field is shown in figure 3.7

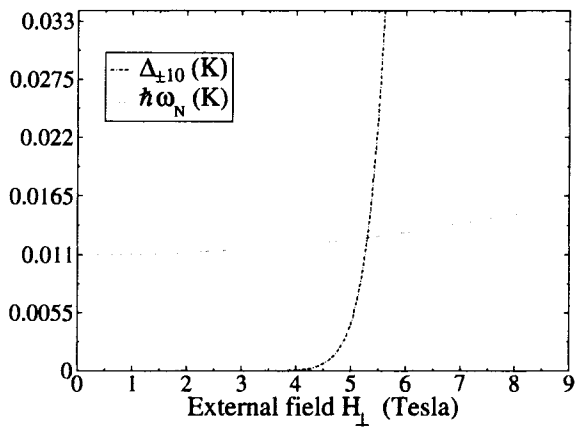

Figure 3.7 The splitting of the ground state in Kelvins and Larmor frequency as a function of transverse magnetic field. Resonance is expected at $H_{\perp} \approx 5.35$ T.

and we can see that at around $H_x = 5.35$ T, tunneling splitting of the ground state $|\pm 10\rangle$ resonates with the nuclear Zeeman splittings. Other resonances are also present for the states $|\pm M\rangle$ ($|M| < 10$) at lower fields, but experiments are performed at low temperatures $T \sim 1.5$ K, whereas $E_{M=\pm 9} \approx 14.4$ K which makes their resonances less

measurable.

In general, the field **H** that acts on the spin may not be oriented purely along the anisotropy axis. A transverse field, can mix spin states from both wells of the anisotropy potential in Eq. (3.4). Therefore, eigenstates of the Hamiltonian can neither be characterized by spin up or down, but rather as a linear combination of the $|+M\rangle$ and $|-M\rangle$. A small parallel field, however, can greatly suppress the mixing and localize each of the states in either of the two wells. As one increases the transverse field, $\mathbf{H}_\perp$, energy states will be delocalized again. This will lead to having two statistically equivalent canting directions for the ground state corresponding to the states $|M = \pm S\rangle$ as shown in figure 3.8 resulting, in general, in two different total Zeeman fields at the nuclear site. We shall denote them as the positive and the negative branches. At low temperatures, it is a good approximation that each of the canting directions for the state $|\nu\rangle$ has the probability of $p_\pm^\nu \equiv |\langle\nu|M = \pm S\rangle|^2$ respectively.

When magnetic fields, H, other than hyperfine are very small, the absolute value of the frequencies for both branches are close in value, which leads to a single frequency line in NMR experiments. However, for larger fields, the two branches start to differ.

In order to obtain the total value of T_1^{-1} we multiply Eq. (3.9) by the statistical weight of the initial state $|\nu\rangle$ and the quantum probability $p_\pm^\nu$ for each of the branches and sum over initial and final states $|\nu\rangle$ and $|\nu'\rangle$. The equation for T_1^{-1} then reads:

$$\begin{aligned}\frac{1}{T_1} &= \frac{\pi\alpha^2 A_{hf}^2}{Z\hbar^2}\sum_{\nu\nu'} p^\nu e^{-\frac{E_\nu}{k_B T}} \times \\ &\left[|\langle\nu'|\,K_+\,|\nu\rangle|^2\,\delta\left(\frac{E_{\nu'}-E_\nu+\hbar\omega}{\hbar}\right)\right. \\ &\left.+\,|\langle\nu'|\,K_-\,|\nu\rangle|^2\,\delta\left(\frac{E_{\nu'}-E_\nu-\hbar\omega}{\hbar}\right)\right] \\ &+2\pi\gamma_N^2 H_{hf}^2\,\langle\delta(\omega)\rangle\sin^2\Theta, \end{aligned} \tag{3.10}$$

Where

$$\langle \delta(\omega) \rangle = \frac{1}{Z} \sum_{\nu} e^{E_\nu / k_B T} \delta_\nu(\omega),$$

and Z is the partition function, and the delta functions are replaced by the Lorentzian distribution function with broadening equal to the inverse of the life time of the electronic state ν due to spin-phonon interaction [36] as follows:

$$\tau_\nu^{-1} = \frac{D^2}{12\rho\pi c^5 \hbar^4} \sum_{\nu'} \frac{\Delta_{\nu'\nu}^3}{e^{\Delta_{\nu'\nu}/k_B T} - 1} \times \left[\left| \langle \nu' | \{S_+, S_z\} | \nu \rangle \right|^2 + \left| \langle \nu' | \{S_-, S_z\} | \nu \rangle \right|^2 \right], \quad (3.11)$$

where D is the same as the anisotropy parameter appearing in Eq. (3.4), $c \approx 2000$ m/s is the phonon velocity and $\rho = 1.83 \times 10^3$ Kg/m^3 is the mass density of the molecule. Note that we have to take into account that when we have a transverse applied field, the states $|\nu\rangle$ are not eigenstates of the S_z operator. Hence the matrix element $\langle \nu' | \{S_\pm, S_z\} | \nu \rangle$ must be calculated explicitly as follows:

$$\langle \nu' | \{S_\pm, S_z\} | \nu \rangle = \sum_M \langle \nu' | M \pm 1 \rangle \langle M | \nu \rangle (2M \pm 1) \sqrt{(S \mp M)(S \pm M + 1)}, \quad (3.12)$$

where $\langle M | \nu \rangle$ is the projection of the state $|\nu\rangle$ into the S_z eigenstate $|M\rangle$ which can be obtained by diagonalizing Eq. (3.4). The calculations of the lifetimes are shown in figures 3.9.

Figure 3.10 shows the calculated T_1^{-1} using Eq. (3.10). To obtain agreement with experiment at low fields, we assumed a large internal transverse field, H_{int} of around 0.52 T distributed uniformly in the molecule's $x - y$ plane. The total transverse field felt by the molecule is therefore, the vector sum if the internal transverse fields and

the perpendicular component of the applied field. As shown in the inset of figure 3.10, when we assume $H_{\text{int}} = 0$, the nuclear relaxation rate enhances abruptly as we turn on the applied transverse field. We can conclude that thermal fluctuations through the spin-phonon bath are too small to account for the nuclear magnetic relaxation. This is not a surprise since the life time of the ground state is longer than that of the first excited state by many orders of magnitude as we can see in figure 3.9.

By including an internal perpendicular field H_{int} of only several hundred of gauss, as one would expect from hyperfine interaction with nuclei and from intermolecular interactions, the nuclear relaxation time can be reduced by a factor of $\sim 10^3$, but it is still longer than observed by a factor of a century. The value $H_{\text{int}} = 0.52$ T needed to fit experiment is surprisingly large if it is to be expected to arise from interaction with nuclei and neighbouring clusters. However, our result is close to the value of ~ 0.4 T obtained by E. del Barco *et al.* in their hole digging experiment [37] which was performed on a single crystal of Mn12-BrAC, another cluster belonging to the family of Mn12-AC magnetic molecules which strictly follows the S_4 symmetry group. This apparently large field may be a attributed to the multi-spin nature of the molecule where an applied field may have less effect on tunneling splitting and quantum spin fluctuation the larger the truncation of Hilbert space [38]. The single spin model is a severe, but justified, truncation of Hilbert space where only states of the $S = 10$ manifold are believed to be relevant to low temperature experiments.

Effect of misalignment of the molecule's easy axis with the laboratory $z-$axis can be taken into account. Such misalignment could be the result of the existence of small internal fields, crystalline misalignment due to non-vanishing terms in Eq. (2.14), and due to direction uncertainty of the applied field. The results are shown in figure 3.10 where the fit is enhanced at larger applied field, as expected.

At transverse field $B_\perp \approx 5.35$ T, the ground state tunneling splitting matches the nuclear Zeeman frequency ω . However, no resonances have been found around such field.

This can be explained by small internal longitudinal fields acting on the electronic spins. Longitudinal fields ranging from 0 to 0.05 T lead to tunneling splittings in the range of 0 to 1.33 K. At low temperatures, the fluctuation of such fields are slow compared to the time scale of the NMR experiment ($\sim 10^{-8}$ s), so that at any time, only a small fraction of molecules is in resonance. In order to take this effect into account, we assumed a small magnetic field in the z direction of about ± 0.015 T (see inset at the bottom right of figure 3.9) which is enough to drive the system out of resonance at all transverse fields.

It is worth pointing out here how accounting for the presence of different isomers affects the results obtained in this chapter where tunneling terms except the internal transverse field term were neglected. There are two types of terms. The terms in Eq. (2.14) introduce tilts of easy axis, which are found to be less than 1° as seen in table 2.3. This is less than the misalignment of the powder. Misalignment of various origins are taken into account as seen in figure 3.10. Note from the figure that misalignment has no effect at zero external field. On the other hand, the terms in Eq. (2.6) and Eq. (2.5) assist the transverse field and promote tunneling. Since most of the molecules are out of resonance in the duration of the NMR pulses, tunneling of the spin is not the main factor responsible for the nuclear magnetic relaxation. In fact, we have performed calculations where second and fourth order anisotropy terms were included. In all cases, fitting for the internal transverse field yield approximately the same value obtained when such terms are neglected.

In conclusion, we used the Moriya approach modified to account for the long life time of the Mn12-AC ground state at low temperature. We have explained the physical origin of the canting term introduced phenomenologically by the authors of Ref. [12]. From the dependence of the ^{55}Mn nuclear magnetic relaxation rate $1/T_1$ on applied transverse field at the low field regime, we argued that thermal fluctuation of the electronic spin caused by the phonon bath can not account for large value of $1/T_1$ at very small applied fields. Such fluctuations must be enhanced by transverse components of the electronic spins,

$K_{\pm}$, with regard to the nuclear Zeeman axis. $1/T_1$ depends strongly on transverse fields when ground state life time due to spin-phonon interaction show very slight dependence on the applied transverse field in the low field regime. Also we related the absence of the expected peak to the presence of internal longitudinal fields. Such field can be of nuclear or intermolecular dipolar term.

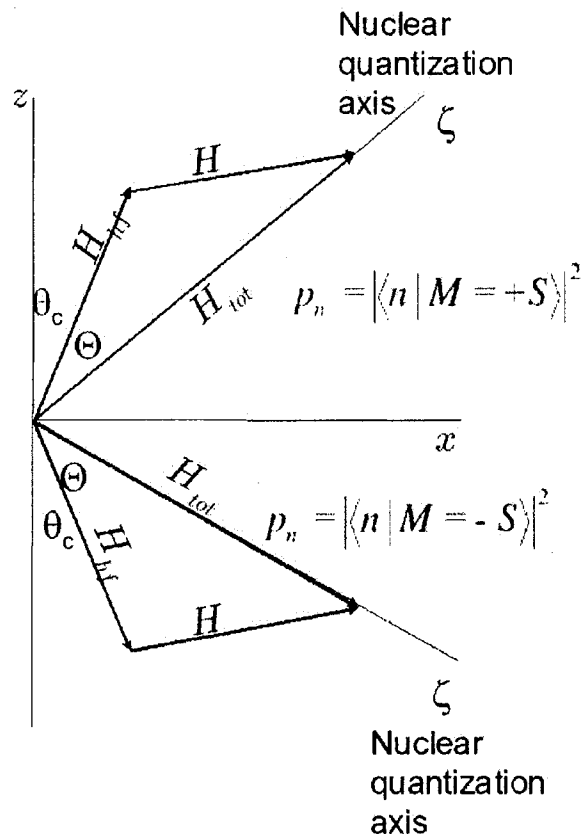

Figure 3.8 Two possible canting schemes due to the two ground state spin directions. Longitudinal components of the field H can lead to two different frequencies corresponding to two different vector sum of the fields.

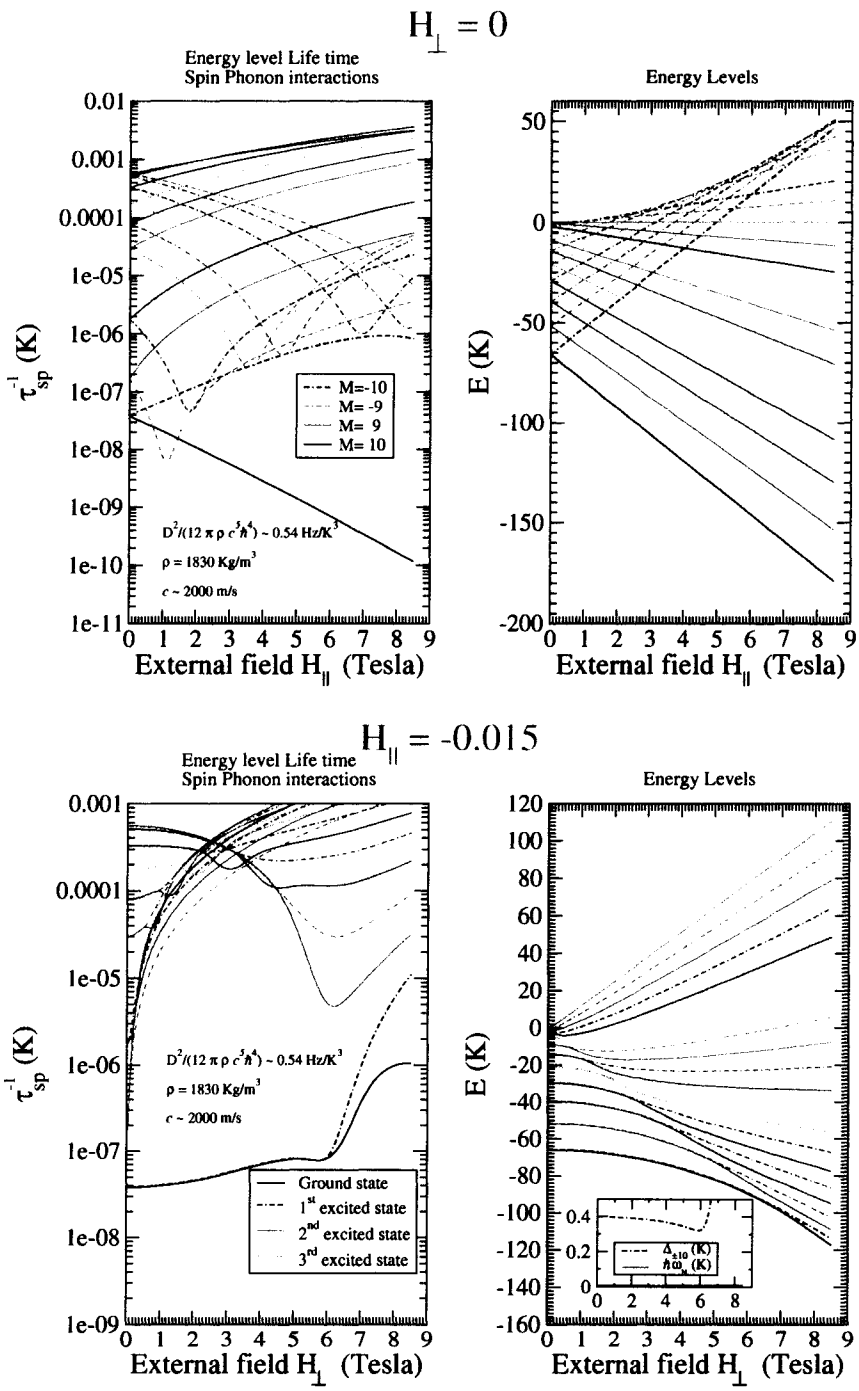

Figure 3.9 (right) Energy spectrum of the Hamiltonian 3.4 vs. longitudinal (top right) and perpendicular(bottom right) applied field. (left) the corresponding reciprocal of energy levels' lifetimes due to spin-phonon interaction calculated using Eq. 3.11. Inset of bottom right figure shows the effect of introducing a small longitudinal field on the tunneling splitting of the ground state.

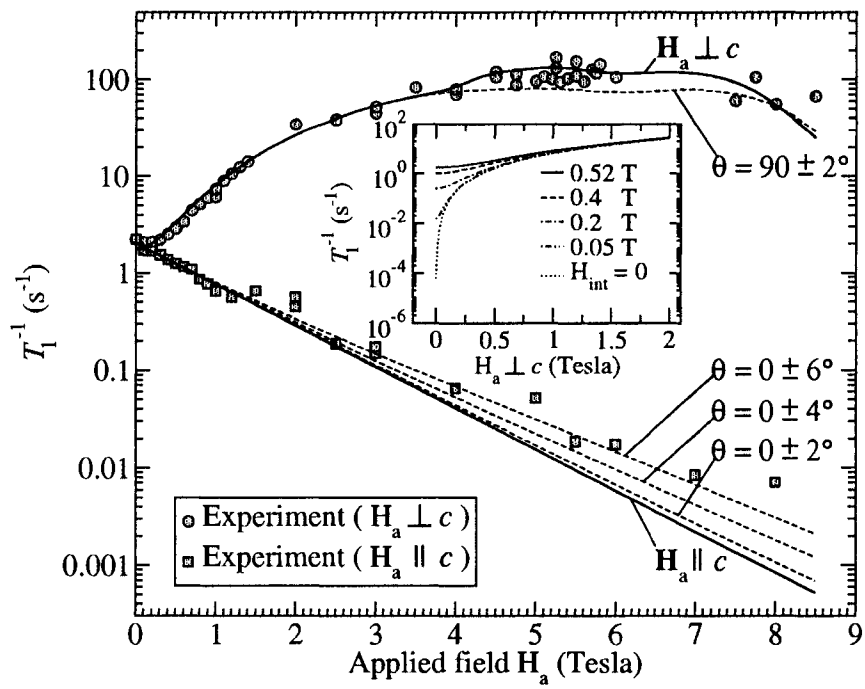

Figure 3.10 $1/T_1$ dependence on applied field, both perpendicular and parallel to the molecule's easy axis c. Dashed lines show the effect of misalignment of the clusters easy axis to the applied field. Inset shows the low field portion of the $1/T_1$ dependence on applied transverse field for different values of internal transverse fields. Experimental data or obtained via private communications with Y. Furukawa.

Chapter4 Tunneling Splitting Calculations and Truncation of Hilbert Space

We calculate the tunneling splittings in a Mn12-AC magnetic molecule taking into account its internal many-spin structure. We discuss the precision and reliability of these calculations and show that restricting the basis (limiting the number of excitations taken into account) may lead to significant error (orders of magnitude) in the resulting tunneling splittings for the lowest energy levels, so that an intuitive picture of different decoupled energy scales does not hold in this case. Possible routes for further development of the many-spin model of Mn12-AC are discussed.

A number of impressive experimental results have been obtained recently, such as thermally assisted tunneling [2, 39], ground state-to-ground state tunneling [40, 41] and topological phase effects in spin tunneling [40]. Quantitative analysis of these experiments is a challenging theoretical problem involving fundamental issues about tunneling phenomena in *mesoscopic* magnetic systems. The basic prerequisite for solving this problem is our ability to evaluate accurately and reliably the energy splittings occurring as a result of tunneling between two (quasi) degenerate levels [42, 43]. At present, carefully designed magnetic relaxation experiments at low and ultra-low temperatures (tens or hundreds of millikelvin) can detect [2, 39] the changes in relaxation time caused by the splittings of order $10^{-2} - 10^{-4}$ K, and even smaller [40], of order $10^{-6} - 10^{-7}$ K. The relaxation time data obtained in these experiments give information (although indirect) about the splitting values, so that predictions of the theoretical models can be compared

with experimental results.

Conventionally, the molecular magnet Mn12-AC is considered as a large single spin $S = 10$ with quasi-degenerate levels $|+M\rangle$ and $|-M\rangle$ split because of tunneling. However, the single-spin Hamiltonian is a phenomenological construct; in reality, this is a many-spin system, consisting of 12 manganese ions coupled by exchange interactions. Here, using Mn12-AC as a well-studied example, we address the problem of reliable many-spin calculation of the tunneling splittings in molecular magnets. Such a calculation is a very complicated task. For example, the Hilbert space of the spin Hamiltonian describing a molecule of Mn12 consists of 10^8 levels, while the smallest tunneling splittings in Mn12-AC are of order of 10^{-10} K (as measured in Ref. [44] for $M = \pm 10$). The brute-force direct calculation of tiny tunneling splittings in this system, even for several low-lying states, is beyond the capabilities of modern computers. The general strategy to solve this problem is to truncate the full Hilbert space thus reducing consideration to a much smaller number of relevant energy levels. This idea, implemented in a rather sophisticated way, forms a basis of several approaches for the evaluation of tunneling phenomena, such as quantum Monte Carlo methods [45], stochastic diagonalization [46], and instanton calculations [47].

To our knowledge, all calculations of the tunneling splittings in molecular magnets starting from realistic Hamiltonians have employed truncation of the Hilbert space in a much more straightforward, and much less justified manner. High-energy basis states, assumed to be irrelevant, are being explicitly excluded from consideration, and only the low-energy part of the spectrum is being taken into account [48]. In this chapter, we calculate tunneling splittings using the many-spin model of Mn12-AC in the reduced 8-spin scheme; examining the accuracy and reliability of this straightforward scheme. We demonstrate that, because of strong Dzyaloshinsky-Moriya (DM) interactions present in Mn12-AC, the splitting values obtained in this way are unreliable. We also consider the sensitivity of the calculated splitting values to variation in the Hamiltonian parameters,

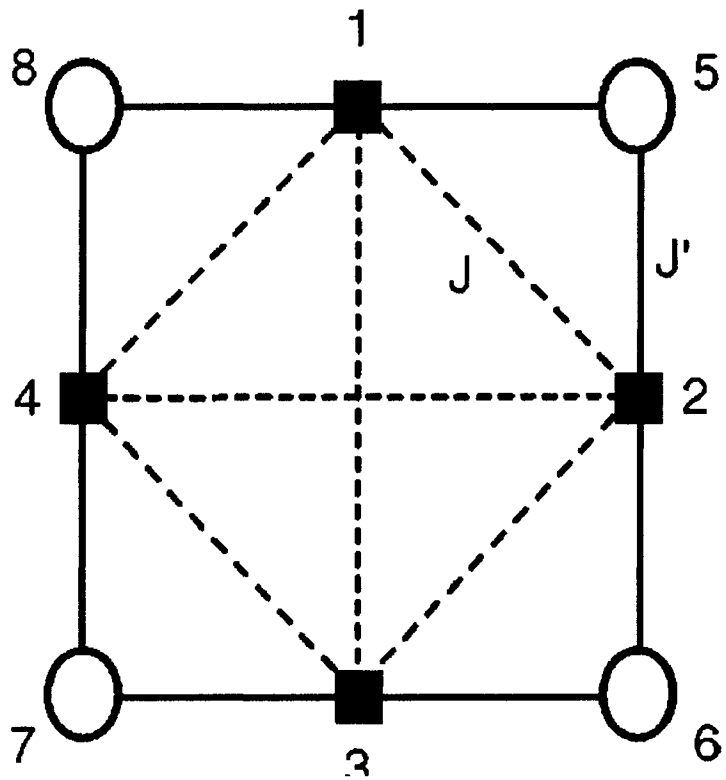

Figure 4.1 The Spin model proposed for the Mn12-AC molecule under the assumption $J_1 \gg J_2$, J_3 and J_4.

and determine the accuracy needed for reliable splittings calculation.

4.1 The 8-Spin model and calculation of tunneling splittings

The cluster Mn12-AC consists of eight Mn^{3+} ions having spin 2 and four Mn^{4+} ions having spin 3/2, coupled by exchange interactions. The total number of spin states in Mn12-AC is 10^8, and a corresponding Hamiltonian matrix is rather large to be treated by modern computers. To overcome this difficulty, we can employ the natural hierarchy of interactions present in Mn12-AC: The antiferromagnetic exchange interactions $J_1 \simeq$ 220 K between Mn^{3+} and Mn^{4+} ions are are assumed to be significantly stronger than all

the others[1] [10], so corresponding pairs of Mn^{3+} and Mn^{4+} ions can be considered as stiff dimers with the total spin $S = 1/2$, thus giving rise to the 8-spin model of Mn12-AC. The range of validity of the 8-spin model, and the corresponding 8-spin Hamiltonian of Mn12 have been considered in Ref. [49]. After examination of different possible interactions, the following Hamiltonian has been proposed:

$$\mathcal{H} = \sum_{\langle i,j \rangle} J_{ij} \mathbf{S}_i \cdot \mathbf{S}_j - \sum_i K_i S_{z,i}^2 + \sum_{\langle i,j \rangle} \mathbf{D}^{ij} \cdot [\mathbf{S}_i \times \mathbf{S}_j], \tag{4.1}$$

where the sum appearing twice in the Hamiltonian run through nearest neighbors. The first term describes isotropic Heisenberg exchange between the spins. The second term describes the single-ion easy-axis anisotropy of large spins (where $K_i = 0$ for the dimer spins). The fourth term represents the antisymmetric DM interactions in Mn12-AC, where $\mathbf{D}^{ij}$ is the DM vector describing the DM-interaction between i-th small spin and j-th large spin. Existence of DM-interactions in Mn12-AC has been suggested in Ref. [50], and their magnitude has been estimated in Ref. [49] based on the neutron scattering data [51]. The molecules of Mn12-AC possess a fourfold rotational-reflection[2] axis (symmetry S_4) imposing restrictions on the DM-vectors $\mathbf{D}^{ij}$, so that DM interactions can be described by only three parameters $D_x \equiv D_x^{1,8}$, $D_y \equiv D_y^{1,8}$, and $D_z \equiv D_z^{1,8}$.

It has been demonstrated [49] that the above model satisfactorily describes a rather wide range of experimental data, such as the splitting of the neutron scattering peaks, results of EPR measurements and the temperature dependence of magnetic susceptibility. Here, for calculations we use the parameter set **A** from Ref. [49]:

$$\begin{aligned} \text{set } \mathbf{A}: \quad & J = 0 \qquad J' = 105\,\text{K} \quad K_i = 5.69\,\text{K} \\ & D_x = 25\,\text{K} \quad D_y = 0 \qquad D_z = -1.2\,\text{K}, \end{aligned} \tag{4.2}$$

[1] The work of this chapter was performed before it was found that J_1 and J_2 are comparable in value (see chapter 5). However, the analysis and calculations presented in this chapter are not affected.

[2] Even though it was found later that Mn12-AC has lower than S_4. the conclusion drawn by the examining the DM interaction will be the same if lower symmetry terms were included.

which also gives a good description of the response of Mn12-AC molecules to a transverse magnetic field (external field applied perpendicular to the easy axis of the molecule). However, this set of parameters should not be considered as being accurately determined, since the amount of the experimental information available is not yet sufficient to achieve particularly reliable parameters. In Hamiltonian 4.1, only the third term, representing the DM interactions, can lead to tunneling:[3] the first two terms conserve the z-projection, M, of the total spin and cannot induce tunneling between levels with different M, while the DM-term mixes levels with different M. In what follows, we will label the energy levels by the value of M. Although it is not an exact quantum number, we can formally consider the DM-interaction as a perturbation, and use perturbation theory terminology.

The following values of the tunneling splittings corresponding to the parameter set 4.2 have been obtained by the diagonalization of the full Hamiltonian matrix (of the size $10^4 \times 10^4$) using quadruple precision arithmetic:

$$\begin{aligned} \Delta E_{\pm 10} &= 1.18 \times 10^{-15}\,\mathrm{K}, \\ \Delta E_{\pm 8} &= 1.06 \times 10^{-11}\,\mathrm{K}, \\ \Delta E_{\pm 6} &= 3.87 \times 10^{-8}\,\mathrm{K}, \\ \Delta E_{\pm 4} &= 2.08 \times 10^{-6}\,\mathrm{K}, \\ \Delta E_{\pm 2} &= 4.17 \times 10^{-2}\,\mathrm{K}. \end{aligned} \tag{4.3}$$

[3]Note that Dzyaloshinsky-Moriya interactions have nonzero matrix elements only for the pairs of levels the have $\Delta M = 0, \pm 1$, but they do not necessarily couple the levels with the same value of the total spin S: It means that the tunneling splittings are governed by the ratio $D_{x,y,z}/J'$, i.e. the tunneling barrier is created primarily by the exchange. This is in contrast with the single-spin model picture, where the tunneling appears due to the anisotropy term $(S_+^4 + S_-^4)$, so that the ratio C/D (introduced in first chapter) determines the splittings, and the tunneling barrier coincides with the anisotropy barrier.

The splittings for odd values of M are not shown: they constantly remain at the level of the numerical precision of the calculations (of order of 10^{-19} K) [52]. In Mn12-AC; these splittings should be zero since the fourfold symmetry[4] of the molecule imposes certain restrictions on the symmetry of the spin Hamiltonian and makes some matrix elements vanish. In the single-spin model of Mn12-AC this property of the spin Hamiltonian is introduced explicitly, by retaining only those operators which possess the required fourfold symmetry. In the many-spin simulations, we obtain the same result independently.

The first question to pose concerns the accuracy of the level splitting evaluation. Parameters of the Hamiltonian are determined with some finite precision, and a small error (say, of the order of several kelvin) affects the level energy by an amount of order of kelvin, which is much larger than the very small value of tunneling splitting (of order of $10^{-10} - 10^{-12}$ K). Does this deprive the calculational results of all meaning? To answer this question, we note that the levels $|+M\rangle$ and $|-M\rangle$ are degenerate due to exact symmetry properties of the spin Hamiltonian, and, in the absence of the DM-term, would be degenerate at any value of parameters. Therefore, the tunneling splittings $\Delta E_{\pm M}$ are governed only by the strength of the interaction which breaks the symmetry, i.e. the DM-interaction. If the parameters of the Hamiltonian are determined with reasonably small *relative* error, and if the numerical calculation is done with sufficient precision, then the *relative* error of the level splittings will also be small. This conclusion is supported by our calculations: a 10% variation in the Hamiltonian parameters leads to the variation in the splitting values at most by a factor of ten, so that accurate determination of the Hamiltonian parameters is necessary for reliable calculation of the tunneling splittings. If only a logarithmic accuracy in the splitting values is needed, then the 10% uncertainty in the Hamiltonian parameters is sufficient.

[4]see foot note on page 46.

4.2 Numerical scheme of truncation of Hilbert space

The description of the Mn12-AC molecule by the 8-spin model requires a full, high-precision diagonalization of the Hamiltonian matrix with dimensions $10^4 \times 10^4$. Solving this problem is rather time-consuming. Matrices of that size can be processed very effectively using Lanczos-type methods, but the application of these methods to the tunneling splitting calculations constitutes quite a difficult problem by itself and pose another important source of error in tunneling splitting calculations. A very large number of iterations is needed to achieve the necessary precision and, in addition, the precision is hard to control when the level separation is very small, so that special techniques are necessary.

Therefore, it is natural first to explore another approach, namely, to omit high-energy basis states, retaining only the low-lying part of the spectrum where basis levels have energies less than some threshold value E_{cut}. This approach has been adopted extensively and in fact, we are not aware of any calculations of tunneling splitting of magnetic molecules done in a different way: calculations based on both the single- and many-spin model [48] have employed this method. Here, we assess the validity of this energy-based truncation approach by considering the dependence of the tunneling splittings $\Delta E_{\pm M}$ for different pairs of degenerate levels $|+M\rangle$ and $|-M\rangle$ on the number of lowest levels N_{low} actually used in calculations (or, in other words, their dependence on the energy threshold E_{cut}).

A brief description of the basis states and how it is used in the strategy of truncating the Hilbert space is in order. We first consider the first exchange term in the Hamiltonian of Eq. (4.1) and construct it using the basis states of individual spins, $|M; m_1, m_2, \ldots, m_8\rangle$. Matrix elements of the first term of the Hamiltonian (4.1) can

only mix basis states of the same value of M as can be seen from the follows:

$$\mathcal{H}^{i,j}_{\text{exch}} = J_{ij}\mathbf{S}_i \cdot \mathbf{S}_j = \frac{J_{ij}}{2}\left(S^i_+ S^j_- + S^i_- S^j_+\right) + J_{ij}S^i_z S^j_z, \tag{4.4}$$

$$\begin{aligned}\langle M'; m'_{k=1\cdots 8}|\, S^i_\mp S^j_\pm \,|M; m_{k=1\cdots 8}\rangle &= \sqrt{(S_i \pm m_i)(S_i \mp m_i + 1)} \times \\ &\quad \sqrt{(S_j \mp m_j)(S_j \pm m_j + 1)} \times \\ &\quad \delta^{m'_i}_{m_i \mp 1}\delta^{m'_j}_{m_j \pm 1}\prod_{k\neq i,j}\delta^{m'_k}_{m_k},\end{aligned} \tag{4.5}$$

and

$$\langle M'; m'_{k=1\cdots 8}|\, S^i_z S^j_z \,|M; m_{k=1\cdots 8}\rangle = m_i m_j \prod_{k=1}^{8}\delta^{m'_k}_{m_k}, \tag{4.6}$$

where we used the fact that:

$$|M; m_{k=1\cdots 8}\rangle = \prod_{k=1}^{8}|m_k\rangle\,. \tag{4.7}$$

Note that the Kronecker delta functions appearing in the Eq. (4.5) and Eq. (4.6) imply that $M = M'$.

This means that the exchange terms are block diagonal in the $|M; m_{k=1\cdots 8}\rangle$ basis and eigenenergies are degenerate with respect to the index M for states belonging to the same total S manifold . We can, then, diagonalize the exchange Hamiltonian within the block of all the spin configurations yielding states with $M = 0$ since it gives *all* energies

Table 4.1 Number of possible configurations for each M block of the exchange Hamiltonian for the 8−spin model.

M	0	±1	±2	±3	±4	±5	±6	±7	±8	±9	±10
Λ_M	1286	1224	1056	824	576	356	192	88	32	8	1

of the system where the projection $M = 0$ can be the $z-$projection of any of the spins from 0 to 10. We shall call this the $M = 0$ block. For the dimer model, where we have four $S = 2$ and four $S = 1/2$ spins, there are 1286 possible states that satisfy the condition $M = \sum m_i = 0$. In table (4.1) we list the total number Λ_M of possible states for each M block of the Hamiltonian. The total number of all possible states is 10 000.

Each of the 1286 energy eigenvalues obtained by diagonalizing the $M = 0$ block corresponds to eigenstates with S ranging from 0 to 10, because $[S^2, \mathbf{S}_i \cdot \mathbf{S}_j] = 0$. We shall label these states as $|S_{\lambda_{M=0}}; M\rangle$, where $\lambda_M = 1, 2, \ldots, \Lambda_M$. The distribution of states is: $(10,1)$, $(9,7)$, $(8,24)$, $(7,56)$, $(6,104)$, $(5,164)$, $(4,220)$, $(3,248)$, $(2,232)$, $(1,168)$, $(0,62)$, where the first number in parenthesis is the value of S and the second is the number of levels with this value of S: With the $2S + 1$ degeneracies included, there are exactly, again, 10 000 states. These are the basis states which are then used to diagonalize the full Hamiltonian, including anisotropy and DM terms.

By knowing the states $|S_{\lambda_M}; M\rangle$ we can build the eigenstates $|S_{\lambda_{M\pm1}}; M \pm 1\rangle$ using the ladder operators $S_\pm$. First we expand the eigenstates of the exchange in terms of the individual spin states using the completeness relation [53]:

$$|S_{\lambda_M}; M\rangle = \sum_{\{m_k\} \in M} |M; m_{k=1\ldots8}\rangle \langle M; m_{k=1\ldots8} |S_{\lambda_M}; M\rangle . \tag{4.8}$$

Then, we apply $S_\pm$ on both sides to get

$$S_\pm |S_{\lambda_M}; M\rangle = \sum_{\{m_k\} \in M} \left(\sum_{i=1}^{8} S_\pm^i \right) |M; m_{k=1\ldots8}\rangle \langle M; m_{k=1\ldots8} |S_{\lambda_M}; M\rangle ,$$

which gives us:

$$|S_{\lambda_{M\pm1}}; M \pm 1\rangle = \sum_{\{m_k\} \in M} \langle M; m_{k=1\ldots8} |S_{\lambda_M}; M\rangle \times$$

$$\sum_{i=1}^{8} \frac{\sqrt{(S_i \mp m_i)(S_i \pm m_i + 1)}}{\sqrt{(S_{\lambda_M} \mp M)(S_{\lambda_M} \pm M + 1)}} |M \pm 1; m_{k\neq i}, m_i \pm 1\rangle , \tag{4.9}$$

Although the last equation looks cumbersome to read, it gives a significant advantage: in order to obtain *all* the eigenstates of the exchange Hamiltonian, we need not diagonalize it in the full space. We only need to diagonalize the $M = 0$ block and build the eigenstates of other blocks in a straight forward manner. Another advantage of Eq. (4.9), is that for each eigenstate $|S_{\lambda_{M=0}}; M = 0\rangle$ obtained from diagonalizing the $M = 0$ block, we can build all relevant $2S + 1$ states belonging the the same manifold S and have $M = -S$ to $M = S$. This means that we have the liberty of choosing any initial states of interest; in particular, those which have their energies less than E_{cut}. For example, If we choose the lowest state only obtained from $M = 0$ block and build the $2S+1$ relevant manifold states, we are basically produce the single spin model discussed in chapter (2). For us to examine relevance of higher energy states to the tunneling splitting calculations, we sort the eigenenergies of the exchange and choose only states which have their energies less than E_{cut} and denote their number to be N_{low}. For each of those states, we use their eigenvectors $\langle M = 0; m_{k=1\ldots8} |S_{\lambda_{M=0}}; M = 0\rangle$ to build the eigenvectors using the recursive Eq. (4.9) as follows:

$$\begin{aligned} \langle M \pm 1; m'_{k=1\ldots8} |S_{\lambda_{M\pm1}}; M \pm 1\rangle \;=\; & \sum_{\{m_k\}\in M} \langle M; m_{k=1\ldots8} |S_{\lambda_M}; M\rangle \times \\ & \sum_{i=1}^{8} \frac{\sqrt{(S_i \mp m_i)(S_i \pm m_i + 1)}}{\sqrt{(S_{\lambda_M} \mp M)(S_{\lambda_M} \pm M + 1)}} \times \\ & \delta^{m'_i}_{m_i\pm1} \prod_{k\neq i} \delta^{m'_k}_{m_k}, \end{aligned} \tag{4.10}$$

where we used the orthogonality relation:

$$\langle M \pm 1; m'_{k=1\ldots8} \, | M \pm 1; m_{k\neq i}, m_i \pm 1 \rangle \;\; = \;\; \delta^{m'_i}_{m_i \pm 1} \prod_{k \neq i} \delta^{m'_k}_{m_k}.$$

Now we can construct a new Hamiltonian matrix where the energies already obtained are the diagonal elements of it and the states expressed in Eq. (4.9) are its eigenstates (Eigenvectors in Eq. (4.10) represent the projection of the eigenstates $|S_{\lambda_M}; M\rangle$on the individual spin basis states $|M; m_{k=1\ldots8}\rangle$). These eigenstates are used to express the second and third terms of the Hamiltonian (4.1) in their basis. This Hamiltonian, which is constructed so that it only contains the unperturbed energies whose value less than E_{cut} can be diagonalized and tunneling splittings of the $E_{\pm M}$ can be obtained.

4.3 Results

We repeated the procedure described in the previous section for different values of E_{cut} (and hence different values of N_{low}). The initial increase in the number of basis states considered, N_{low}, leads to an overall increase in $\Delta E_{\pm M}$ accompanied by oscillations (see Fig. (4.2)). After N_{low} achieves the value of about 700, the oscillations have become small and $\Delta E_{\pm M}$ versus N_{low} exhibits a plateau. This saturation lead in Ref. [48] to the conclusion that the resulting values give the actual splittings with sufficient accuracy. But this conclusion is wrong. A further increase of the number of levels leads to a resurrection of the oscillations at $N_{\text{low}} = 1200$, with a quite pronounced jump in $\Delta E_{\pm M}$ for $N_{\text{low}} = 1700$. For a larger number of levels, the situation repeats itself: the values of the splittings reach another plateau, then oscillations appear again with a subsequent jump, etc. We have traced this behavior up to $N_{\text{low}} = 3000$, which is already 1/3 of the total number of levels. The observed behavior of $\Delta E_{\pm M}$ is, in our opinion, a very clear signal that energy-based truncation of the Hilbert space is not a good strategy for the

computation of tunneling splittings: it gives unreliable results.

The rather sharp jumps in the tunneling splittings as discussed above and illustrated in Fig. (4.2) are associated with the inclusion of basis states with large S values. Because of the selection rule for the DM term ($S \rightarrow S \pm 1$), the $S = 10$ ground state only couples with $S = 9$ states. States with smaller S values affect the splittings more indirectly by coupling with other states which eventually couple to the ground state. While the states with large S cause jumps in the splitting values, there are few of them, and the smaller coupling of smaller S states still is significant because of the cumulative effect of so many states (see the distribution given above). Therefore, the evaluation of tunneling splittings for a general system possessing strong DM interactions requires consideration of sufficiently large portion of Hilbert space.

It is noteworthy that the same truncation method works rather well for calculations of the energies of well-separated levels. To compare the model against most of the experiments, it suffices to know the positions of the levels with much less precision, usually an error < 0.1 K is already adequate. This level of precision can be obtained by taking into account $N_{\text{low}} \sim 1000$ levels (i.e. 1/10 of the total Hilbert space). Even using $N_{\text{low}} \sim 500$; the error in the level position is < 1 K even for the states of energy at about 60 K. Therefore, the matrix-truncation approach is adequate for fitting the model parameters to experimental data. But the calculations of the tunneling splittings should be done using the full Hamiltonian matrix.

4.4 Discussion

We have shown that truncating the Hilbert space leads to large errors in the calculated values of tunneling splittings. But actually, any sensible Hamiltonian is inevitably obtained due to some truncation of the Hilbert space. For example, Hamiltonian (4.1) can be considered as a result of the two-step procedure [54, 55]: (i) projection of the real

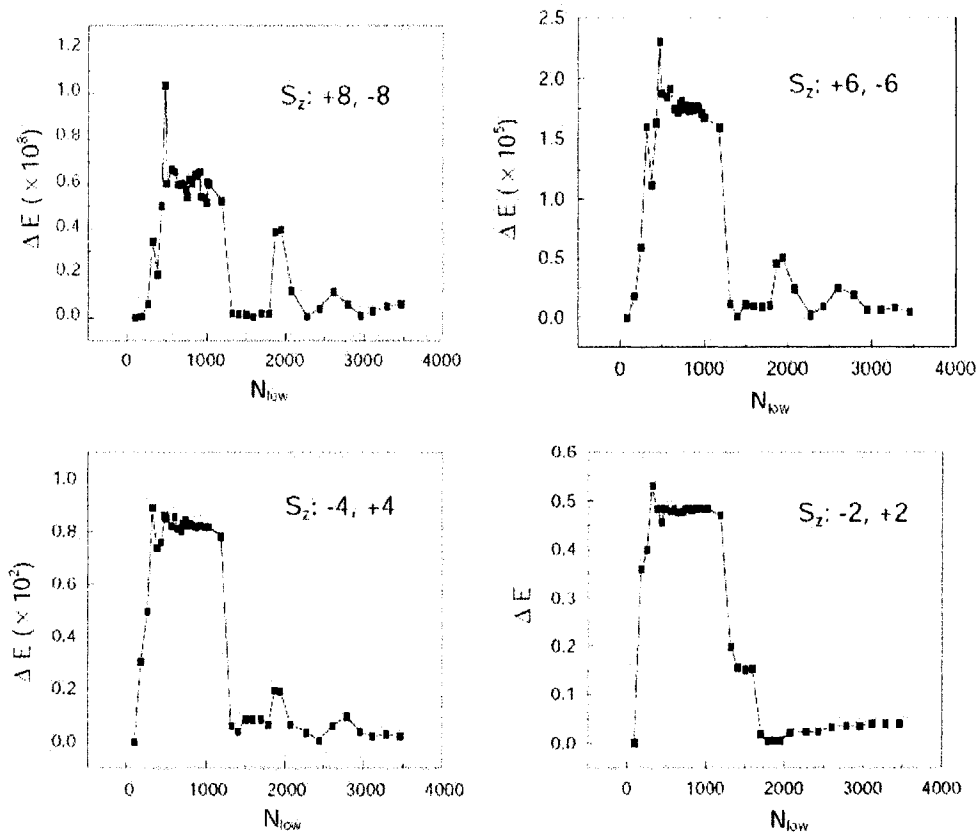

Figure 4.2 Dependence of the tunneling splittings $\Delta E_{\pm M}$ (in kelvin) versus the number of levels taken into account in the many-spin calculations. The parameter set **A** (see text) has been used for calculations. The results for $M = 8$, 6, 4, and 2 are presented. tunneling splittings for the levels with odd M are zero because of the symmetry properties of the spin Hamiltonian.

many-electron Hamiltonian onto the subspace of suitably chosen single-electron orbital states, yielding a general spin Hamiltonian of the molecule and (ii) projection of the resulting spin Hamiltonian onto the subspace of the 8-spin model. This procedure is usually justified (at least, at the heuristic level) by invoking some kind of perturbation or WKB-theory arguments, and corresponds to an intuitive idea of different, practically independent energy scales.

However, in the case of the tunneling splittings, we see that very different energy scales significantly affect each other. Why do the same arguments not work if we truncate the 8-spin Hamiltonian? In our opinion, this takes place because the conditions of the applicability of WKB-reasoning (or similar arguments based on perturbation theory) are not satisfied. The spin of the system $S = 10$ is too small, so that the instanton action [42] on the trajectories corresponding to the 8-spin model is not large enough. Indeed, for systems with well-separated levels, the quasi-classical approximation usually already works reasonably for a total spin $S \sim 2 - 3$. However, as has been demonstrated [56], to apply the same type of arguments to the splitting calculations, the (normalized) instanton action S_I should exceed the value of 12. For the model employed in Ref. [56], this corresponds to the system with a total spin (more exactly, with the total antiferromagnetic vector) of order of several thousand. Thus, the tunneling splittings, in general, appear to be much more sensitive to the method of calculation than the level energies themselves, and conditions for applicability of the conventional WKB-reasoning are considerably more stringent (though for Mn12-AC they can of course be different from the condition $S_I > 12$). Qualitatively, this agrees with our observations (see sections 4.1 and 4.3). Even a rather severe truncation of the Hilbert space has a minor effect on the level energies, while correct values of the tunneling splittings require a diagonalization of the full Hamiltonian.

Briefly, these arguments can be expressed in a rather obvious form: the 8-spin model is not "macroscopic enough" to justify the truncation of the Hilbert space by some

WKB or similar perturbation approach. In this case the intuitive picture of different independent energy scales is misleading.

This conclusion raises important questions, namely, is the 8-spin model, being the result of the truncation of, e.g., 12-spin Hamiltonian, sufficient to predict reliably the tunneling splittings (or, in other words, is the 12-spin model "macroscopic enough" to be truncated)? What is the minimal model allowing the splittings to be calculated correctly? We believe that these are key questions, not only for Mn12-AC but for the whole class of magnetic molecules. For this purpose, *ab initio* calculations of the exchange and anisotropic intramolecular interactions in Mn12-AC could be very useful. Also, reliable experimental data for the tunneling splittings would obviously be of great value for further development.

In conclusion, we have calculated the tunneling splittings in Mn12-AC on the basis of the 8-spin model proposed earlier [49]. We have shown that rather accurate knowledge of the Hamiltonian parameters is needed for the accurate splitting calculations; although, for logarithmic accuracy, 10% error in the parameters can be tolerated. Furthermore, we have demonstrated that a reliable calculation of the tunneling splittings for a system with strong DM interactions requires the use of the full Hamiltonian matrix. We have explicitly shown that an energy-based Hilbert space truncation scheme can be successfully used for the determination of the level energies, but leads to erroneous results when applied to the splitting calculations.

Chapter5 Exchange Couplings For The Full Spin Model

Lately, there have been several attempts to describe the exchange picture of the Magnetic Molecule known as the Mn12-Ac. In this chapter, we use the Davidson Algorithm to explore the properties of the low energies of the Mn12-Ac using the most recently suggested exchange parameters. Our results show that introducing small single ion anisotropy terms to the exchange interactions affects the energy spectrum in a non-trivial manner in contrast to the common belief, suggesting that the exchange picture of the molecule is insufficient and more general Hamiltonian must be considered.

The Hamiltonian of the ground state of Mn12-AC molecule has been constructed phenomenologically by retaining terms allowed by molecule's symmetry. When in the ground state, the Mn12-AC molecule can be considered as a large rigid spin $S = 10$ whose multiplets are split in zero field due to a global anisotropy term such that the transition from the ground state to the first excited state is $\sim$ 14.4 K as detected in inelastic neutron scattering [51, 57] and by EPR measurements [18] leading to an estimated anisotropy energy barrier of approximately 65 K [10]. This model has been widely used to understand the experimental results. However, it is inadequate when trying to fully explain many of these results such as the neutron scattering [51], megagauss field magnetization [58, 59, 60], and optical absorption experiments [61], which reflect internal structure properties of the Mn12-AC molecule. We also demonstrated in the chapter (4) that tunneling splitting calculations require the full Hilbert space that represents the spin system. Spin tunneling rates at level *anticrossings* depend on tunneling splitting values, therefore, predictions of the size of jumps in the magnetic hysteresis loop of the

Mn12-AC cluster based on the single spin model are not reliable since the single spin model has the Hilbert space truncated to include the $S = 10$ ground state manifold only and discards all other states even those which lie within the anisotropy barrier of the ground state $S = 10$ manifold [62].

As we can see from the diagram in figure 2.2, neighboring Mn ions are coupled to each other via exchanges through different types of oxygen bridges and by acetate bridges. As a result, both ferromagnetic and antiferromagnetic exchange interactions may be present. It is also interesting that the interaction between the four Mn^{4+} are not all equal. The Mn^{4+} ions are arranged in the four corners of a cubane (distorted cube, see figure 5.1) while the other four corners are occupied by the oxygen providing superexchange bridges between the manganese ions. As a result, the four Mn^{4+} ions form a distorted tetrahedron with four short edges (J_3) and two longer ones (J_3'). Although the distortion of exchange pathways is moderate, it is found that the calculated coupling parameters, J_3 and J_3' turn out very different [63] as we can see from the J parameter set 5 in table (5.1).

5.1 Exchanges as published up to date.

Considering the internal structure of the magnetic molecules becomes essential for understanding the properties involving excited states of different total spin values and tunneling splittings within the ground state manifold. As first suggested by Sessoli *et al.* [10], the antiferromagnetic exchange coupling J_1 (see figure 2.2) is much larger than all other exchanges, so corresponding pairs of ions can be treated as dimers of a rigid spin $\frac{1}{2}$ leading to a simpler model of the Mn12-AC molecule consisting of 8-spins which was discussed in chapter (4) (see Refs. [49] for detailed study of this model). However none of the exchange sets propose in Ref. [10] yields a ground state of $S = 10$. Raghu *et al.* [64] has tested variants of the sets published in the Ref. [10] keeping the assumption that

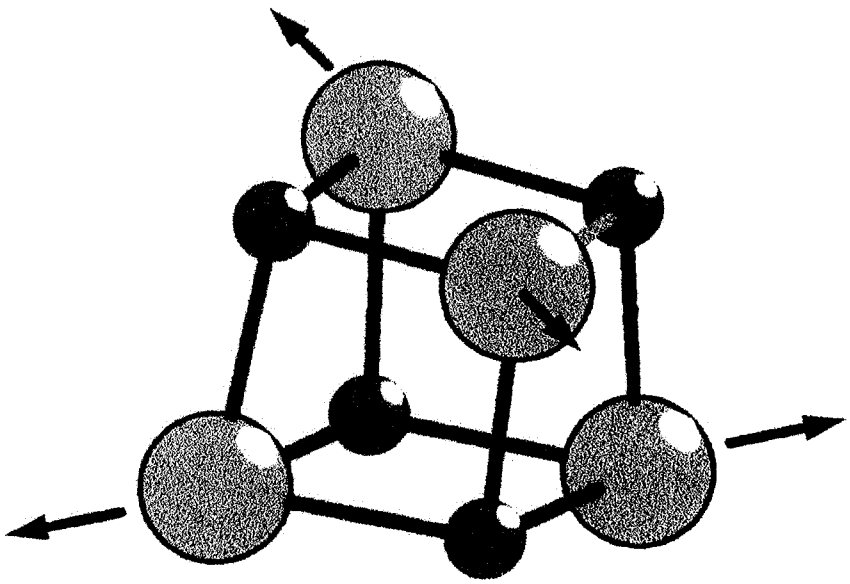

Figure 5.1 Sketch of the arrangement of the manganese and oxygen ions in the inner cubane of Mn12-AC molecule. Arrows show the directions of the displacement of the Mn^{4+} ions which lead to the formation of the inner cubane instead of the perfect cube. Figure and caption are taken from Ref. [63].

Table 5.1 The exchange coupling parameters suggested by previous authors. Except in the set LDA+U , it is assumed that $J_2' = J_2$, $J_3' = J_3$, and $J_4' = J_4$. Positive exchanges are antiferromagnetic.

Set Name	J_1	J_2	J_2'	J_3	J_3'	J_4	J_4'
1- Raghu *et al.* [64] set E	215	85		85		-64.5	
2- Regnault *et al.* [70]	119.43	118.22		-8.06		22.84	
3- Park *et al.* [67]	115	84		-4		17	
4- Chaboussant *et al.* [57]	67.2	61.8		7.8		5.6	
5- LDA(+U=4 eV). [68]	50	43	37	8	3	10	6

J_1 is larger than all other exchanges and give an $S = 10$ ground state. The set that was recommended by the authors and used for subsequent calculations are shown in table (5.1), set 1.

The internal properties of the Mn12-AC molecule were investigated by using *ab initio* electronic structure. So far, density-functional computations of the electronic structure for Mn12-AC molecule have been carried out within the local-density approximation (LDA) [65], generalized gradient approximation (GGA) [66, 67], and LDA+U approximation, taking into account the on-site Coulomb Correlations [63, 68].

Other recent attempts considered Heisenberg Model for multi-spin interactions between the Mn12-AC ions in the cluster. The exchange parameters were tuned mainly to reproduce the 35 K energy gap between the ground state multiplet ($S = 10$) and the excited state of $S = 9$ [64, 67, 69, 70], and to reproduce the molecule magnetization curves [70]. In addition to previous data, exchange interactions were tuned to reproduce high temperature susceptibility curves as well as for higher energies obtained by neutron scattering [57]. As a result, we have in hand several exchange sets which vary appreciably from each other and are listed in table (5.1).

5.2 The Heisenberg Hamiltonian for Mn12-AC

The exchange coupling scheme of the Mn12-AC molecule is of the form:

$$\mathcal{H}_{\text{exch}} = \sum_{<i,j>} J_{ij}\mathbf{S}_i \cdot \mathbf{S}_j, \tag{5.1}$$

where the sum is taken over the nearest-neighbour pairs, hence there is no double counting of the interactions. The exchange parameters J_{ij} (positive for antiferromagnetic interaction) are defined as in the schematic diagram in figure 2.2.

The Hilbert space of this spin Hamiltonian is 100×10^6 in dimension. Approximation methods are necessary to carry out the calculations in such huge dimensionality. Since we are interested in the lowest lying states, Lanczos and Davidson algorithms are very suitable for the task. In the Hamiltonian (5.1), the total spin, S, is a conserved integer quantity and takes the values: $0 \leq S \leq 22$. We use the rotational symmetry implied by the Spin Hamiltonian (5.1) to treat it as a block diagonalized matrix and thus reduce the Hilbert space into smaller ones. If we use the z-projection of the total spin, M, as a conserved quantity, we can have 45 blocks and each block will represent a certain value of M where $-22 \leq M \leq 22$. Since it is well established that the ground state energy of the molecule corresponds to total spin $S = 10$, the ground state should be expected by diagonalizing Eq. (5.1) in any of the subspaces corresponding to $M = 0, \pm 1, \pm 2, ... \pm 10$.

The largest Hilbert space in the reduced scheme, is 8 581 300 corresponding to $M = 0$ subspace and the smallest one among those which contain the ground state is 817 176 corresponding to $M = \pm 10$ subspaces. Recent studies have implemented further reduction of the Hilbert space using the S_4 point group and spin parity symmetries of the molecule [57, 64, 69]. The later method was not employed in the calculations represented in this chapter.

As mentioned in the previous section, Eq. (5.1) was diagonalized in each of the spin

Table 5.2 The results of diagonalizing Eq. (5.1) using exchange parameters listed in table 5.1. The total spin, S, and the degeneracy, d, are shown in the table next to energies. Energies are in Kelvins Results of previous authors are shown in square brackets only in case of discrepancy with our results. Question marks indicates that results were not reported by previous authors.

Set	E_g	S_g	d_g	E_1	S_1	d_1
1	0	10	1	35.8[35.1:]	9	2[?]
2	0	10	1	34.95[35]	9	2[?]
3	0	10	1	39.13[40.53]	9	2[?]
4	0	10	1	28.48	9	2
5	0	10	1	6.82	9	2
	E_3	S_3	d_3	E_4	S_4	d_4
1	63.5[missing]	8	1[?]	84.5[82.4]	7	2[?]
2	67.21[67]	9	1[?]	68.12[?]	8[?]	1[?]
3	77.12[80.74]	9	1[?]	78.39[?]	8[?]	1[?]
4	56.52[?]	8[?]	1[?]	58.49[?]	8[?]	1[?]
5	14.13	8	1	15.46	8	1

projection $M = 0, \pm1, \pm2, ..., \pm10$ subspaces using exchange parameter sets which have been suggested by the previously mentioned works and are listed in table (5.1). Diagonalization has been performed using the well known Davidson Algorithm [71] which computes the lowest (or highest) energy eigenvalues with their eigenvectors (often called eigenpairs) up to the desired precision. The algorithm, as well as the Lanczos algorithm, is very susceptible to hidden symmetries in the matrix and has the potential to skip eigenpairs depending on initial guess(es). The Davidson algorithm is capable of computing degenerate eigenstates natively and providing their distinct eigenvectors which can be used to calculate further properties of the system.

Table (5.2) shows our results of diagonalizing Eq. (5.1) using each of the sets published in table (5.1). The results obtained in references are shown in square brackets only when they differ from ours. One can see that our results coincide with the ones published by authors of Ref. [57] (set 4), though they have not reported the energies

coming from the subspace $M = \pm 8$. Aside from the missing energy from Ref. [64] (set 1) and the mismatching spin value of the second excited state in Ref. [70] (set 2), our results are within $1-3$ Kelvins of the previously published results for the sets $1-3$ which may be justified since those authors have reported approximate values of exchanges.

In the following, we will examine the effect of introducing single ion anisotropies on the energy spectrum of the Hamiltonian in Eq (5.1) using the last two sets in tables (5.1) and (5.2) and comment on the results in the light of neutron scattering data [51, 57].

5.3 Effect of single-ion anisotropies on Exchange Hamiltonian.

Recently, using detailed X-Ray diffraction analysis at low temperature, Cornia *et al.* [23] has shown that the anisotropy axes of the Mn^{3+} ions within the cluster are not parallel due to Jahn-Teller distortion of the ligands surrounding the Mn^{3+} ions. Furthermore, due to 50% possibility that acetic acids interact with these ligands, we have two possible variants of each of the anisotropy parameters for each of the Mn^{3+} ions. Cornia *et al.* [23] calculated such parameters for each of the Mn^{3+} ions which we will use in further calculation of the energy spectrum.

To take the single-ion anisotropies into account, we write the Hamiltonian of the system in the form:

$$\begin{aligned} \mathcal{H} &= \sum_{<i,j>} J_{ij}\mathbf{S}_i \cdot \mathbf{S}_j + \sum_i K_i S_{i,z}^2 \\ &\quad + \sum_i E_i \left(S_{i,x}^2 - S_{i,y}^2\right) + \cdots, \end{aligned} \tag{5.2}$$

where K_i (E_i) is the easy axis (transverse) anisotropy parameter of the i-th Mn ion. The transverse terms in the Hamiltonian (5.2) lead to small values of tunneling splittings. Furthermore, for each Mn ion, E_i is considerably smaller than the longitudinal anisotropy

parameters K_i, less than 10% [23]. They can be safely treated as perturbation parameters and hence we concentrate on the first two terms in Eq. (5.2). In this work, we use the longitudinal anisotropy parameters K_i for each of the Mn^{3+} ion type calculated in the Crystal's reference frame for one of the six isomers (n=2 trans as labeled in Ref. [23]). The values of resultant K_i are shown in table (5.3).

With the transverse terms neglected, one still can diagonalize the matrix $\mathcal{H}$ in Eq. (5.2) in the reduced scheme as described in section 5.2. The operator $S_{i,z}^2$ commutes with the z-projection of the total spin S_z therefore the quantity $S_z = M$ is conserved. The resultant states of this Hamiltonian are a mix of different S values, since the total spin operator does not commute with first two terms of $\mathcal{H}$. As will be shown, however, the mix is small and the characterization of ground and low excited states with the spin value S is still valid.

The first results which we introduce are the average moments of each of the Mn ions calculated in the ground state before and after adding the anisotropy parameters (see table (5.4)). Except for the first set, we can see the results from direct diagonalization of the exchange model compare very well to the known values of the spin moments deducted from experiment and the DFT calculations and the effect of including the anisotropies on the Mn ion moments is only of the order of $1 - 3\%$. This is a confirmation of the belief that the large amount of reduction of the Mn^{4+} is related to the strong exchange coupling between the Mn (I) and Mn (II) [66].

Energy spectrum resulting from diagonalizing Eq. (5.2) using anisotropy parameters in table (2.2) in each subspace $M = 0, \pm 1, \pm 2, \ldots \pm 10$ is shown in figure 5.2. We used

Table 5.3 Magnetic anisotropy along crystal's easy axis for the four inequivalent site of Mn^{3+} ions.

	Mn2A	Mn2B	Mn3A	Mn3B
K_i(K)	-4.7	-5.08	-2.86	-2.77

Table 5.4 The expectation value of the moment, $\langle S_z^i \rangle / S_i$, in the ground state calculated using eigenvectors of the exchange Hamiltonian 5.1 (column a for each Mn ion type) and the Hamiltonian 5.2 (column b) using each of the five exchange sets in table 5.1 and anisotropies in table 2.2 (for the isomer n=2 trans). For comparison, listed are the results from references: [11] polarized neutron diffraction experiment (PND), [32] ^{55}Mn nuclear magnetic resonance (NMR), and [66] calculations based on the density functional theory (DFT).

	Mn^{4+}		Mn^{3+}(II)		Mn^{3+}(III)	
PND	$78 \pm 4\%$		$92 \pm 4\%$		$94 \pm 3\%$	
NMR	76%		85%		85%	
DFT	86%		90%		90%	
	(a)	(b)	(a)	(b)	(a)	(b)
Set 1	60.1%	61.4%	79.6%	80.2%	90.5%	90.9%
Set 2	83.1%	83.8%	95.5%	95.7%	91.9%	92.2%
Set 3	82.4%	83.3%	93.2%	93.6%	93.6%	93.9%
Set 4	80.8%	82.1%	93.6%	94.2%	92.0%	92.5%
Set 5	79.0%	81%	91.9%	92.8%	92.4%	93%

the lowest two energies in each M subspace to fit for the single spin Hamiltonian (2.2) for zero applied field and got the results shown in the insets of each spectrum of figure 5.2. The first excited energy and energy barriers are 14.7 K 76.2 K (14.2 K and 64.2 K) for set 4 (set 5).

Chaboussant, in Ref. [57] argued that the global anisotropy parameters D and A should have the same values for different manifolds which have the same S value. However, from our results, we can see that this is true as long as the states do not involve strong mix of different S values. For the case of the exchange set 4, we can see that adding anisotropy term into the exchange Hamiltonian, leads to very small mixing that the argument holds true (see annotations in figure 5.2), while for the case of exchange set 5, mix gets larger for lower M values leading to different global parameters even for manifolds of the same approximate value of S.

The α lines appearing figure 5.2 are the transitions from the ground state to excited states which satisfy the neutron selection rules $\Delta M = 0, \pm 1$ and $S = 0, \pm 1$. while both exchange sets produce relatively the same value for the first transitions from the state $|10, \pm 10\rangle$ to the state $|10, \pm 9\rangle (E_{\alpha_1})$, they differ in the next transitions. The lowest $S = 9$ manifolds are at 42.4 K (α_2) and 43.3 K (α_3) for the set 4, while they are much lower for the case of exchange set 5, at 20.5 K (α_2), 21.5 K (α_3) and 23.4 K (α_4). Then there is a single $S = 9$ state at 58.3 K (α_4) for set 4 while it appears at 41 K (α_5) for set 5. Set 5 then gives two other states at 64.6 K (α_6) and 64.7 K (α_6). Then set 5 also gives again another state at 94 K (α_7) while set 4 yields three energies, 101.4 K (α_5), 128.5 K (α_6) and 128.7 K (α_6).

Comparing with experiment, we see that set 5 gave better estimates of the ground state global anisotropy parameters, the first excited energy within the ground state manifold and the energy barrier. However, the transitions it predicts at energies $20-24$ K have not been observed experimentaly [51, 57]. The broad energy observed around 29 K in in experiment [51, 57] is attributed to phonon excitations and are not considered of a

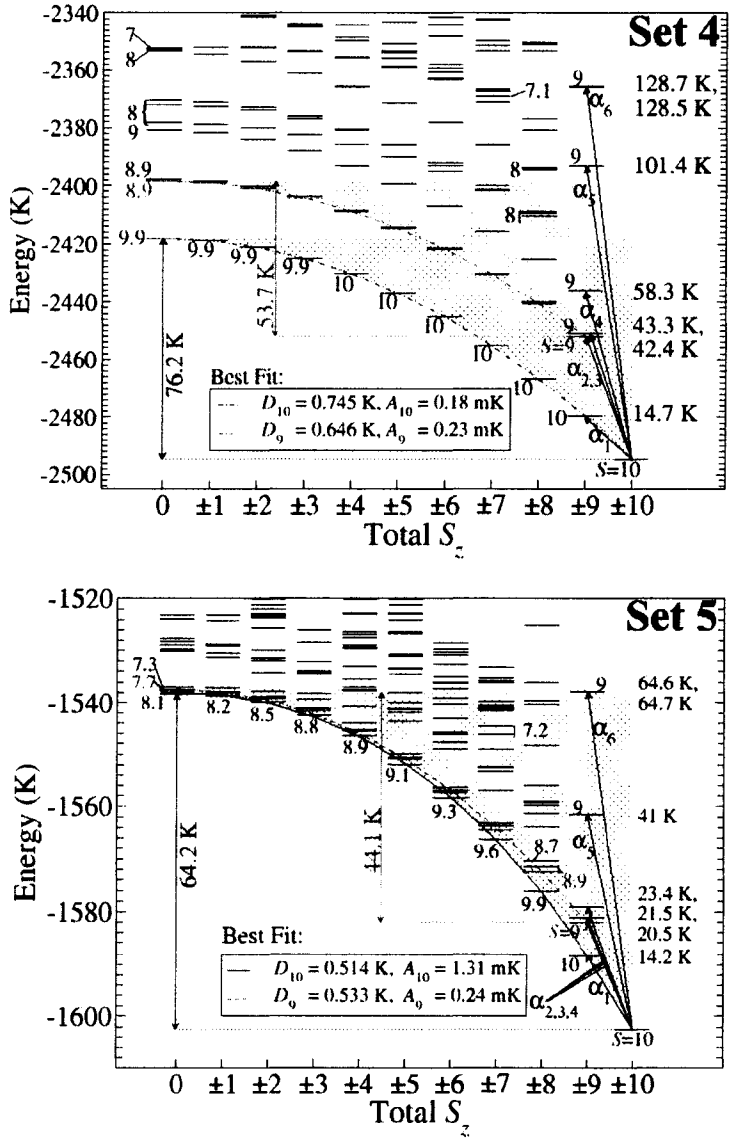

Figure 5.2 Lowest energy levels of Eq. (5.2) within each of the $S_z = 0, \pm1, \pm2, ..., \pm10$ blocks resulting from using sets 4 (top) and 5 (bottom) and including single ion anisotropies from table 5.3. Some levels are annotated by their expectation value of S to show the degree of spin state mixing. The α lines show low energy expected transitions from the ground state as allowed by selection rules in the neutron scattering experiment. The lowest manifolds $S = 10$ and $S = 9$ spectrum were fit for the anisotropy Hamiltonian $-DS_z^2 - AS_z^4$ and the parameter values of the fit are shown in the boxes.

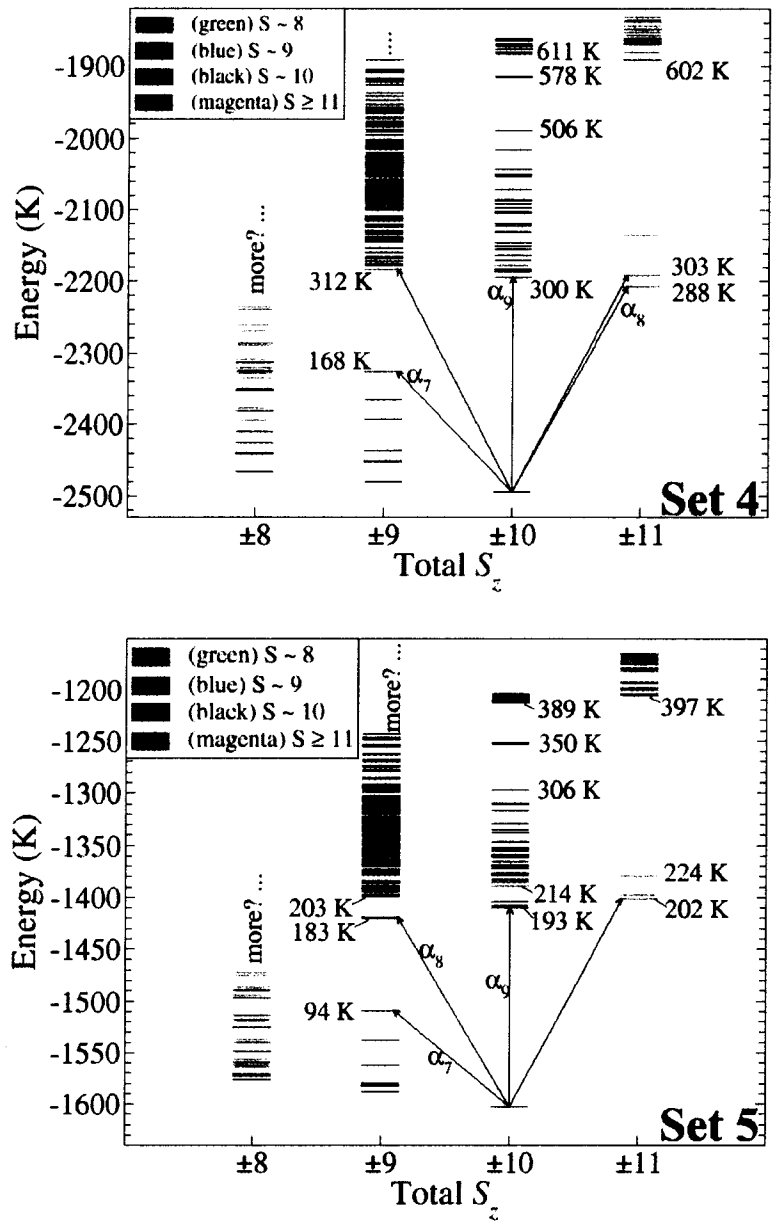

Figure 5.3 Higher scale of energy levels of Eq. 5.2 within each of the $S_z = 0, \pm 1, \pm 2, ..., \pm 10$ blocks resulting from using sets 4 (top) and 5 (bottom) and including single ion anisotropies from table 5.3. The α lines show some of the expected transitions from the ground state as allowed by selection rules in the neutron scattering experiment.

magnetic origin. The energy transitions at about $40-44$ K predicted by both sets 4 and 5, are also not observed in neutron scattering [51, 57], even though it has been observed by electron paramagnetic resonance experiments [62]. This may be explained by their small neutron scattering cross section. The energies $58-65$ K predicted by sets 4 and 5 are close in value to the well observed two peaks at 61 K and 72 K. The peak at 94 K predicted by set 5 is close for the two observed peaks observed at 93 K and 101 K, while the peaks $128.5-128.7$ K predicted by set 4 are higher than the nearest next observed peak, at 112 K, by around 20 K but are closer to the unconfirmed one, at 122 K (see figure 4-b and table II in Ref. [57]).

We then show higher energy transitions, up to 600 K (set 4) and 400 K (set 5) in figure 5.3. After α_7, the very next expected transition predicted is to a state $S = 11$ at 288 K for set 4 ($S = 9$ at 183 K for set 5). This introduces energy gaps between neutron peaks. According to set 4, the gap is around 120 K from 168 K to 288 K while according to set 5, the gap is $\sim$ 90 K from 94 K to 183 K. In experiment, a gap in the neutron peaks is observed from $122-313$ K.

There is one last thing to mention regarding figure 5.3. For both sets 4 and 5, after the transitions labeled as α_9, the states belonging to $M = \pm 10$ ($S = 10$ and 11) subspace are relatively dense and those belonging to $M = \pm 9$ ($S = 9$, 10 and 11) are quasi-continuum. This is in sharp contrast with experiment where only few transition were recognised up to $E = 500$ K. Summery of the results mentioned above are compared with experimental results [57] in figure 5.4.

In summery, we can see that the overall agreement between the predicted neutron transition and the exchange+anisotropy Hamiltonian is less than satisfying especially at higher energies. The reason for the observed inconsistency between neutron scattering experiments and the exchange model may be due to the fact that exchange coupling parameters depend on the relative orientation of the interacting spins. This shades the question of the reliability of using exchange interactions to describe a large quantum

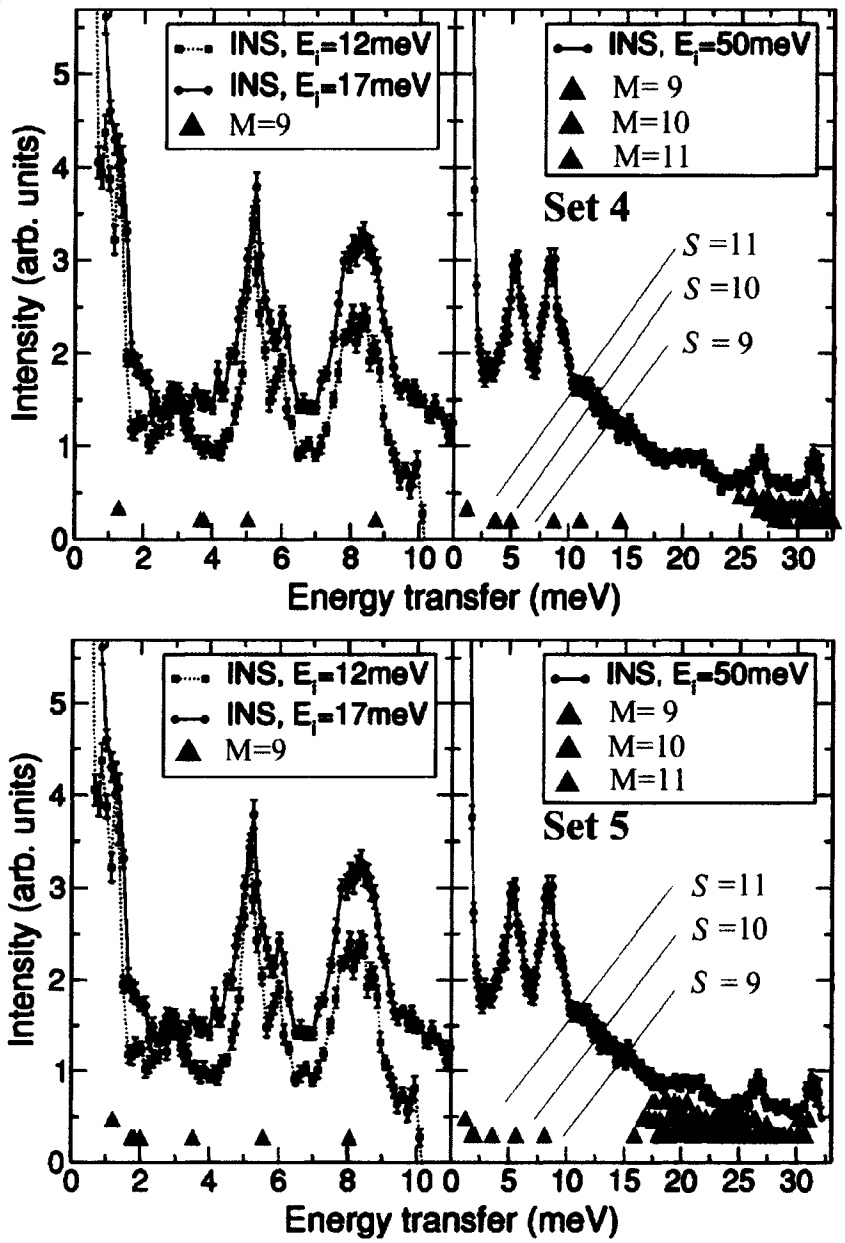

Figure 5.4 Results of exact diagonalization (ED) and results of inelastic neutron scattering experiment at 8 K cited from Ref. [57] for each of the sets 4 (top) and set 5(bottom). Left figures are for lowere energy regime and right figures show energy transfers up to 370 K. Energies are shown in meV where 1 meV == 11.6 K.

system which contains huge number of possible spin configurations. To explain this, we find that, for example, set 5, gives closer results to experiment for the ground state. This is not surprising if we recall that the LDA+U calculation yielding set 5 are done on the ground state spin configuration of the Mn12-AC molecule, while set 4 was obtained by fitting for high temperature susceptibility curves. As mentioned in Ref. [63], calculating the exchanges for the completely ferromagnetic spin configuration, yielded exchanges that are $20-30\%$ different than those obtained for the ground state spin configuration. On other words, the exchange parameters are likely to depend on the orientation of the individual spins, so that a Heisenberg model with fixed exchange couping parameters may be of limited validity.

Another source of discrepancy between exchange model with anisotropy and experiments, is the fact that we ignore the DM interaction which are of order of $10-20\%$ of exchange coupling parameters [49]. Also in this analysis, we ignored the fact that even for the transitions allowed by the neutron scattering selection rules $\Delta M = 0, \pm 1$ and $S = 0, \pm 1$, the cross section for such transitions could be small due to small matrix elements of the spin operators between the initial (ground state) and final state.

Chapter6 General Summary

In this thesis, we have covered a broad range of model representations of the single-molecular magnet Mn12-AC, from the single-spin model in which the molecule's constituent moments are strongly coupled to form a rigid giant ferrimagnetic spin $S = 10$ to the full-spin model where all 12 moments are taken into account.

The single-spin Hamiltonian is phenomenologically constructed to describe the system in the ground state in the relevant temperature regime. We have applied this model in chapter 3 in order to explain the ^{55}Mn magnetic nuclear relaxation dynamics at low temperature $T = 1.5$ K. The dynamics of the nuclear relaxation is driven mainly by the fluctuation of the local magnetic field felt by the nucleus perpendicular to the orientation of its moment. By using the single-spin model for studying the nuclear relaxation time in the presence of an applied field, we needed to parametrize the internal transverse fields felt by the molecule rather than using real field values expected (500 G at most) from the molecule's environment. A large value of the field parameter is found ($\sim$ 5000 K) to reproduce experimental results. Since the Mn12-AC molecule has large anisotropy, magnetic fields perpendicular to the anisotropy easy axis and less than 50 kG are perturbations to the axial Hamiltonian of the system, but crucial in calculating properties arising from the spin fluctuations. We have found that determining transverse internal fields by analysing experiments depends crucially on the spin model used in the analysis.

In chapter 4, we examined the effect of simplifying the spin model on tunneling properties of the Mn12-AC using the 8−spin model by introducing off-diagonal Hamiltonian terms. We used a scheme in which we can, for example, neglect all energy levels which

have energies above a threshold value in the calculations. In other words, truncation of Hilbert space. We found that tunneling splittings of the ground state depends non-monotonically on the number of levels included. The correct tunneling splitting were not predicted even when the number of included levels were close the total dimension of the Hilbert space. This supports the findings of chapter 3. Although tunneling of the spin has a different nature from spin fluctuations considered in chapter 3, both critically depend on the spin configuration of or spin degrees of freedom.

Once we learned the areas where simplification schemes are not adequate to describe the properties of the Mn12-AC magnetic molecule, we started attacking the problem from the full-spin model representation. We included the terms known to date to construct the Hamiltonian matrix and employed the Davidson algorithm in obtaining the lowest energies (up to $400-600$ K) of the Hamiltonian. This is a promising to obtain reliable estimates of various exchanges, like Dzyaloshinsky-Moriya interactions. HOwever researching in parameter space is still too computationally demanding to adequately attack the general 12-spin model. It is worth noting here that although the Davidson algorithm is developed only to give lowest energies of the system, the simplification scheme it follows is not based on truncation of Hilbert space as the one used in chapter 4. The algorithm encapsulates the whole Hamiltonian matrix into smaller matrices which are easier to diagonalize in contrast to the truncation algorithm which totally ignores the contribution coming from matrix elements of the Hamiltonian related to the excluded energy states. Employing the Davidson algorithm to calculate tunneling splittings of Mn12-AC ground states is still very difficult even for modern computer because of the high precision such calculations require. Such difficulty may be overcome in the next few years when computer hardware becomes faster and storage media become cheaper. But such algorithms can be used very efficiently nowadays for smaller systems (even for calculations of high precision tunneling splittings.

BIBLIOGRAPHY

[1] J. R. Friedman, M. P. Sarachik, J. Tejada and R. Ziolo, Phys. Rev. Lett. **76**, 3830 (1996).

[2] J. R. Friedman, M. P. Sarachik, J. Tejada, J. Maciejewski and R. Ziolo, J. Appl. Phys. **79**, 6031 (1996).

[3] J. M. Hernández, X. X. Zhang, F. Luis, J. Tejada, J. R. Friedman, M. P. Sarachik and R. Ziolo, Phys. Rev. B **55**, 5858 (1997).

[4] R. Sessoli and D. Gatteschi, Angew. Chem., Int. Ed. **42**, 268 (2003).

[5] J. Tejada, E. M. Chudnovsky, E del Barco, J. M. Hernandez and T. P. Spiller, Nanotechnology **12**, 181 (2001).

[6] K. W. H. Stevens, Proc. Phys. Soc. **65**, 209 (1952).

[7] A. Abragam and B. Bleaney, "Electron Paramagnetic Resonance of Transition Ions" (Dover, New York, 1986).

[8] T. Lis, Acta Crystallogr., B **36**, 2042 (1980).

[9] A. Caneschi, D. Gatteschi, R. Sessoli, A. L. Barra, L. C. Brunel and M. Guillot, J. Am. Chem. Soc. **113**, 5873 (1991).

[10] R. Sessoli, H. -L. Tsai, A. R. Schake, S. Wang, J. B. Vincent, K. Folting, D. Gatteschi, G. Christou, and D. N. Hendrickson, J. Am. Chem. Soc. **115**, 1804 (1993).

[11] R. A. Robinson, P. J. Brown, D. N. Argyriou, D. N. Hendrickson, and S. M. Aubin, J. Phys. - Condens. Mat. **12**, 2805 (2000).

[12] Y. Furukawa, F. Borsa, T. Sasaki, N. Kobayashi, and D. Gatteschi, Phys. Rev. B **67**, 0064426 (2003).

[13] M. A. Novak, R. Sessoli, A. Caneschi and D. Gatteschi, J. Magn. Magn. Mater. **146**, 211 (1995).

[14] M. A. Novak and R. Sessoli, in "Quantum Tunneling of Magnetization", edited by L. Gunther and B. Barbara (Kluwer, Dordrecht, 1995), p. 171.

[15] C. Paulsen, J.-G. Park, B. Barbara, R. Sessoli and A. Caneschi, J. Magn. Magn. Mater. **140-144**, 379 (1995).

[16] C. Paulsen and J.-G. Park, in "Quantum Tunneling of Magnetization", edited by L. Gunther and B. Barbara (Kluwer, Dordrecht 1995), p. 189.

[17] I. Mirebeau,1 M. Hennion, H. Casalta, H. Andres, H. U. Güdel, A. V. Irodova, and A. Caneschi, Phys. Rev. Lett. **83**, 628 (1999).

[18] Y. Zhong, M. P. Sarachik, J. R. Friedman, R. A. Robinson, T. M. Kelley, H. Nakotte, A. C. Christianson, F. Trouw, S. M. J. Aubin, and D. N. Hendrickson, J. Appl. Phys. **85**, 5636 (1999).

[19] A. L. Barra, D. Gatteschi, and R. Sessoli, Phys. Rev. B **56**, 8192 (1997).

[20] Y. Zhong, M. P. Sarachik, J. Yoo, and D. N. Hendrickson, Phys. Rev. B **62**, R9256 (2000).

[21] P. Langan, R. Robinson, P. J. Brown, D. Argyriou, D. Hendrickson, and G. Christou, Acta Crystallogr. Sect. C **57**, 909 (2001).

[22] A. Cornia, A. C. Fabretti, R. Sessoli, L. Sorace, D. Gatteschi, A. L. Barra, C. Daiguebonne, T. Roisnel, Acta Crystallogr. Sect. C **58**, 371 (2002).

[23] A. Cornia, R. Sessoli, L. Sorace, D. Gatteschi, A. L. Barra, and C. Daiguebonne, Phys. Rev. Lett. **89**, 257201 (2002).

[24] A. Messiah, Quantum Mechanics I, translated by G. M. Temmer (North-Holland Pub. Co, Amsterdam; Hohn Wiley & Sons, Inc, NY 1964) p. 339.

[25] A. L. Barra *et al.*, Angew. Chem., Int. Ed. Engl. **36**, 2329 (1997).

[26] A. Bencini, I. Ciofini, and M.G. Uytterhoeven, Inorg. Chim. Acta **274**, 90 (1998).

[27] D. Gatteschi and L. Sorace, J. Solid State Chem. **159**, 253 (2001).

[28] F. Hartmann-Boutron, P. Politi, and J. Villain, Int. J. Mod. Phys. B **10**, 2577 (1996).

[29] E. del Barco, A. D. Kent, E. M. Rumberger, D. N. Hendrickson and G. Christou, Phys. Rev. Lett. **91**, 047203 (2003).

[30] del Barco, A. D. Kent, S. Hill, J. M. North, N. S. Dalal, E. M. Rumberger, D. N. Hendrickson, N. Chakov, and G. Christou, Preprint cond-matt/0404390, (2005).

[31] T. Moriya, Prog. Theor. Phys. **16**, 23 (1956).

[32] T. Kubo, T. Goto, T. Koshiba, K. Takeda, and K. Awaga, Phys. Rev. B **65**, 224425 (2002).

[33] Y. Furukawa, K. Watanabe, K. Kumagai, F. Borsa, and D. Gatteschi, Phys. Rev. B **64**, 104401 (2001).

[34] T. Goto, T. Koshiba, T. Kubo, and K. Awaga, Phys. Rev. B **67**, 104408 (2003).

[35] N. Bloembergen, E. M. Purcell and R. V. Pound, Phys. Rev. **73**, 679 (1948).

[36] M. N. Leuenberger and D. Loss, Phys. Rev. B **61**, 1286 (2000).

[37] E. del Barco, A. D. Kent, N. E. Chakov, L. N. Zakharov, A. L. Rheingold, D. N. Hendrickson, and G. Christou, Phys. Rev. B **69**, 020411(R) (2004).

[38] H. De Raedt, A. H. Hams, V. V. Dobrovitsky, M. Al-Saqer, M. I. Katsnelson, and B. N. Harmon, J. Magn. Magn. Mater. **246**, 392 (2002).

[39] L. Thomas, F. Lionti, R. Ballou, D. Gatteschi, R. Sessoli, B. Barbara, Nature **383**, 145 (1996).

[40] W. Wernsdorfer, R. Sessoli, Science **284**, 133 (1999);
W. Wernsdorfer, T. Ohm, C. Sangregorio, R. Sessoli, D. Mailly, C. Paulsen, Phys. Rev. Lett. **82**, 3903 (1999).

[41] C. Sangregorio, T. Ohm, C. Paulsen, R. Sessoli, D. Gatteschi, Phys. Rev. Lett. **78**, 4645(1997).

[42] J. L. van Hemmen, A. Suto, Physica B **141**, 37 (1986).

[43] M. Enz, R. Schilling, J. Phys. C **19**, 1765 (1986).

[44] B. Barbara, L. Thomas, F. Lionti, I. Chiorescu, A. Sulpice, J. Magn. Magn. Mater. **200**, 167 (1999);
I. Chiorescu, R. Giraud, A.G.M. Jansen, A. Caneschi, B. Barbara, Phys. Rev. Lett. **85**, 4807 (2000).

[45] V. A. Kashurnikov, N. V. Prokof'ev, B. V. Svistunov, M. Troyer, Phys. Rev. B **59**, 1162 (1999).

[46] H. De Raedt, M. Frick, Phys. Rep. **231**, 107 (1993);
H. De Raedt, W. Fettes, K. Michielsen, in: M. P. Nightingale, C.J. Umrigar (Eds.),

"Quantum Monte Carlo Methods in Physics and Chemistry" (Kluwer Academic Publishers, Amsterdam, 1999).

[47] V. V. Dobrovitski, B. N. Harmon, J. Appl. Phys. **83**, 6599 (1998).

[48] M. Al-Saqer, V. V. Dobrovitski, B. N. Harmon, M. I. Katsnelson, J. Appl. Phys. **87**, 6268 (2000).

[49] M. I. Katsnelson, V. V. Dobrovitski, B. N. Harmon, Phys. Rev. B **59**, 6919 (1999).

[50] B. Barbara, W. Wernsdorfer, L. C. Sampaio, J. G. Park, C. Paulsen, M. A. Novak, R. Ferré, D. Mailly, R. Sessoli, A. Caneschi, K. Hasselbach, A. Benoit and L. Thomas, J. Magn. Magn. Mater. **140-144**, 1825 (1995).

[51] M. Hennion, L. Pardi, I. Mirebeau, E. Suard, R. Sessoli, and D. Gatteschi, Phys. Rev. B **56**, 8819 (1997).

[52] J. H. Wilkinson, "The Algebraic Eigenvalue Problem" (Clarendon Press, Oxford 1965). (Extended precision calculations where done on a Cray C90, using 28-digit arithmetics and checked against 33-digit calculations of 1000 1000 problems on a Pentium III processor.)

[53] J. J. Sakurai, "Modern Quantum Mechanics", Rev. Ed. edited by S. F. Tuan (Addison-Wesley 1994).

[54] D. C. Mattis, "The Theory of Magnetism" (Harper & Row, New York 1965).

[55] K. Yosida, "Theory of Magnetism" (Springer, Berlin, New York 1996).

[56] G. Levine, J. Howard, Phys. Rev. Lett. **75**, 4142 (1995).

[57] G. Chaboussant, A. Sieber, S. Ochsenbein, H.-U. Güdel, M. Murrie, A. Honecker, N. Fukushima, B. Normand, Phys. Rev. B **70**, 104422 (2004).

[58] V. V. Platonov, B. Barbara, A. Caneschi, D. A. Clark, C. M. Fowler, D. Gatteschi, J. D. Goettee, I. A. Lubashevsky, A. A. Mukhin, V. I. Plis, A. I. Popov, D. G. Rickel, R. Sessoli, O. M. Tatsenko, and A. K. Zvezdin, (unpublished);
B. Barbara, D. Gatteschi, A. A. Mukhin, V. V. Platonov, A. I. Popov, A. M. Tatsenko, and A. K. Zvezdin, in Proceeding of Seventh International Conference on Megagauss Magnetic Field Generation and Related Topics, Sarov, 1996, (1997), p.853.

[59] A. K. Zvezdin, I. A. Lubashevskii, R. Z. Levitin, V. V. Platonov, and O. M. Tatsenko, Phys. Usp. **41**, 1037 (1998).

[60] D. Gatteschi and R. Sessoli, "Magnetism: Molecules to Materials III", edited by J. S. Miller and M. Drillon (Wiley-VCH, Weinheim, 2002).

[61] S. M. Oppenheimer, A. B. Sushkov, J. L. Musfeldt, R. M. Achey, and N. S. Dalal (unpublished).

[62] K. Petukhov, S. Hill, N. E. Chakov, K. A. Abboud, and G. Christou, Phys. Rev. B **70**, 054426 (2004).

[63] D. W. Boukhvalov, A. I. Lichtenstein, V. V. Dobrovitski, M. I. Katsnelson, B. N. Harmon, V. V. Mazurenko, and V. I. Anisimov, Phys. Rev. B **65**, 184435 (2002).

[64] C. Raghu, Indranil Rudra, Diptiman Sen, and S. Ramasesha, Phys. Rev. B **64**, 064419 (2001).

[65] Z. Zeng, D. Guenzburger, and D. E. Ellis, Phys. Rev. B **59**, 6927 (1999).

[66] M. R. Pederson and S. N. Khanna, Phys. Rev. B **59**, 693 (1999).
M. R. Pederson and S. N. Khanna, Phys. Rev. B **60**, 9566 (1999);
M. R. Pederson and S. N. Khanna, Chem. Phys. Lett. **307**, 253 (1999);

[67] Kyungwha Park, Mark R. Pederson, and C. Stephen Hellberg Phys. Rev. B **69**, 014416 (2004).

[68] D. W. Boukhvalov *et al.* to be published.

[69] Indranil Rudra, S. Ramasesha, and Diptiman Sen, Phys. Rev. B **64**, 014408 (2002).

[70] N. Regnault, Th. Jolicoer, R. Sessoli, D. Gatteschi, and M. Verdaguer, Phys. Rev. B **66**, 054409 (2002).

[71] E. R. Davidson, J. Comput. Phys. **17** , 87 (1975);
E. R. Davidson, Comp. Phys. Comm. **53**, 49-60 (1989).